Nuclear FAK aggravates CD8$^+$ T cell exhaustion via the SP1-IL-6 axis in colorectal cancer

Hao Kong[1, %], Xiangji Wu[1, %], Qingxin Yang[1, %], Chunwei Wu[1, %], Xin Yu[1], Jie Yang[1], Dai Xie[1], Yu Dai[1], Lang Chen[4], Panpan Ma[4], Siqi Dai[1], Libin Huang[5], Chong Chen[1], Peng Mi[1], Yong Peng[1,8], Hubing Shi[7], Dunfang Zhang[1], Nengwen Ke[2], Zongguang Zhou[5], Dan Cao[6], Bing Hu[9], Ping Wang[1, *], Lu Chen[3*], Yun-Hua Liu[4*], Hong Jiang[1, 2, *, #]

[1]Department of Biotherapy, State Key Laboratory of Biotherapy and Cancer Center, West China Hospital, Sichuan University, Chengdu 610041, China.

[2]Department of Pancreatic Surgery, West China Hospital, Sichuan University, Chengdu 610041, China.

[3]Key Laboratory of Birth Defects and Related Diseases of Women and Children of MOE, Department of Laboratory Medicine, State Key Laboratory of Biotherapy, West China Second University Hospital, Sichuan University, Chengdu 610041, China.

[4] Department of Surgical Oncology of the Second Affiliated Hospital, and Department of Pathology & Pathophysiology, Zhejiang University School of Medicine, Hangzhou 310058, China.

[5]Laboratory of Digestive Surgery, State Key Laboratory of Biotherapy and Cancer Center, Sichuan University, Chengdu 610041, China.

[6]Abdominal Oncology Ward, Division of Medical Oncology, Cancer Center, State Key Laboratory of Biotherapy, West China Hospital, Sichuan University, Chengdu 610041, China

[7]Institute for Breast Health Medicine, State Key Laboratory of Biotherapy, West China Hospital, Sichuan University and Collaborative Innovation Center, Chengdu 610041, China, 610041

[8]Frontiers Medical Center, Tianfu Jincheng Laboratory, Chengdu 610212, China

[9]Department of Gastroenterology and Hepatology, Digestive Endoscopy Medical Engineering Research Laboratory, West China Hospital, Sichuan University, Chengdu 610064, China

Lead contact

[%] These authors contributed equally.

*Corresponding authors: Hong Jiang, hjiang@scu.edu.cn; Yun-Hua Liu, yunhualiu@zju.edu.cn; Lu Chen, luchen@scu.edu.cn; and Ping Wang, pingw1202@gmail.com

SUMMARY

Although immune checkpoint blockade (ICB) therapy has shown promise in colorectal cancer patients with high microsatellite instability (MSI-H), response rates remain low for the majority of patients. Key challenges include the exhaustion of $CD8^+$ T cells and the presence of immunosuppressive cells within the tumor microenvironment. By integrating digital spatial profiling and scRNA sequencing, we found that the tumor-intrinsic activation of focal adhesion kinase (FAK) was strongly correlated with the heterogeneity and exhaustion of $CD8^+$ T cells within the spatial context of the tumor microenvironment and correlated with patient survival. Pharmacological inhibition or genetic loss of FAK enhanced antitumor immune responses and synergistically potentiated αPD-1 and αTIM-3 immunotherapy by augmenting $CD8^+$ T cell cytotoxicity and restoring exhaustion in preclinical models of colorectal cancer. Mechanistically, nuclear FAK was found to regulate SP1/IL-6-mediated T cell exhaustion and the transcription of proinflammatory cytokines/chemokines. These findings underscore FAK's pivotal role in $CD8^+$ T cell exhaustion within the immunosuppressive tumor microenvironment, suggesting that FAK is a promising target for advancing cancer immunotherapy.

INTRODUCTION

The treatment of colorectal cancer remains challenging despite advances in multimodal therapy, such as radiation, chemotherapy, and surgery.[1–3] While these approaches improve local disease control, the high distant recurrence rate of nearly 30% and substantial side effects underscore the need for novel therapeutic strategies.[4,5] Immunotherapy has revolutionized cancer treatment for several malignancies, such as melanoma, but has shown limited benefit in colorectal cancer, particularly in microsatellite stable (MSS) tumors.[6,7] Only a small portion of patients with high microsatellite instability (MSI-H) in colorectal cancer, estimated to be approximately 15%, are eligible for immunotherapy targeting PD-1, PD-L1, or CTLA-4.[8–10] Most colorectal cancers are microsatellite stable (MSS) and are not responsive to immunotherapies.[11,12] This disparity highlights the urgent need for innovative immunotherapeutic approaches tailored to colorectal cancers.

Studies have shown that a unique tumor microenvironment characterized by fibrotic stroma, exhaustion of $CD8^+$ tumor-infiltrating lymphocytes (TILs), and extensive infiltration by immunosuppressive cell populations contributes to the failure of therapies.[13–17] However, the heterogeneity and exhaustion of $CD8^+$ T cells within the spatial context of the tumor microenvironment and their correlation with treatment response and patient survival are still largely unknown.[18] Moreover, the mediators driving $CD8^+$ T cell exhaustion and limiting the response to immunotherapy in colorectal cancer are still elusive,[19] representing significant challenges in cancer immunotherapy.[20] A better understanding of these mediators is needed to develop more effective immunotherapies for colorectal cancer and improve patient outcomes.

To address these challenges, we performed digital spatial profiling (DSP) analysis[21] integrating single-cell RNA sequencing datasets of 64 human CRC tissues and 36 normal tissues[22] to elucidate the spatial heterogeneity and functional characteristics of $CD8^+$ TILs. Our findings revealed that the activation of focal adhesion kinase (FAK) correlates with TIL heterogeneity and exhaustion within the tumor microenvironment. Using MC38 and CT26 mouse models of colorectal cancer, we demonstrated that pharmacological inhibition or genetic loss of FAK enhances antitumor immune responses by suppressing SP1/IL-6-mediated T cell exhaustion. Importantly, targeting FAK with an inhibitor enhances the efficacy of αPD-1 and αTIM-3 immunotherapy by boosting the cytotoxicity of tumor-resident $CD8^+$ T cells and reversing exhaustion states in preclinical models. These results suggest that FAK inhibition represents a promising strategy for improving immunotherapy outcomes in human colorectal cancer patients.

RESULTS

Characterizing the immune microenvironment in human colorectal cancer through single-cell transcriptional and spatial proteomic profiling

To evaluate the tumor immune microenvironment (TIME) in human colorectal cancer (CRC), we reanalyzed published single-cell RNA sequencing (scRNA-seq) data from 62 individuals (34 MMRd and 28 MMRp) with primary untreated tumors and adjacent normal colon tissue from 36 individuals,[22] aiming to identify transcriptomic signatures (**Fig. 1a**). By scrutinizing 35 key

TIME-related genes (immune cell markers, immune checkpoints, tumor cell markers and fibroblast markers) (**Supplementary Table 1**), we established an immuno-oncology profile across different colorectal tumor subtypes (**Fig. 1b**). Overall, colorectal cancer tissues exhibited a more complex immune composition than adjacent normal tissues, reflecting immune infiltration heterogeneity. Specifically, while MMRd tumors had greater TIL infiltration than MMRp tumors, as reported previously,[11,23] both tumor subtypes presented signs of TIL exhaustion within the TIME, irrespective of TIL infiltration levels or MMR deficiency status.

Next, we conducted in-depth spatial proteomics on tumor tissues from 9 selected CRC patients (1 MMRd and 8 MMRp) along with adjacent normal colon tissue from 1 patient, aiming to thoroughly explore the spatial TIME of human CRC. The 116 circular regions of interest (ROIs) were categorized into three spatial types (intratumoral, proximal and distal) based on their spatial features (**Extended Data Fig. 1a, b**). Supported by the clustering of T cell markers, these 9 tumors were assigned to 3 TIME subtypes (inflamed, excluded and desert) (**Fig. 1c upper panel and Extended Data Fig. 1c**). Consistent with the scRNA-seq results, inflamed tumors exhibited increased infiltration of immune cells, including $CD8^+$ T cells, particularly in the intratumoral region (**Fig. 1c, lower panel**). More importantly, we observed high expression of immune checkpoints (ARG-1, IDO-1, TIM-3, PD-1, LAG-3 and CTLA-4) in regions enriched with $CD8^+$ T cells across all three TIME subtypes, indicating a tendency toward exhaustion among $CD8^+$ TILs (**Fig. 1c**).

To identify the predominant factor that determines the functional and spatial heterogeneity of TILs among those 9 tumors, we compared proteins that were differentially expressed between every two TIME subtypes of the same histological region. Compared with those in adjacent normal tissues, significantly elevated levels of exhaustion markers, notably TIM-3 and PD-1, were detected in the intratumoral region (**Extended Data Fig. 1d, e, f**). Subsequently, we established an exhaustion scoring system using a set of classic checkpoint genes (*PDCD1*, *HAVCR2*, *TOX*, *LAG3*, *TIGIT*, *EOMES* and *ENTPD1*) (**Fig. 1d**) to quantify T cell exhaustion and found a significantly greater T cell exhaustion score in tumors (**Fig. 1e**). When applied to bulk RNA-seq data from external colorectal cancer patient cohorts, the exhaustion scoring system demonstrated remarkable clinical value, as patients with higher exhaustion scores in these

datasets experienced poorer survival outcomes than those with lower scores (**Fig. 1f**). Together, these findings suggest that intratumoral T cells in colorectal cancers often exhibit signs of exhaustion compared to those in adjacent normal tissues, irrespective of MMR deficiency status or TIME subtype.

Spatial TIL exhaustion is associated with tumor-intrinsic FAK activation

To explore potential drivers of T cell exhaustion, we integrated single-cell RNA sequencing (scRNA-seq) data to compare gene expression profiles between tumor and normal tissues (**Fig. 2a**). Differential expression analysis highlighted significant changes in several signaling pathways, including negative regulation of immune processes, cytokine production, and notably, the progression of focal adhesion, prominently represented by *PTK2* (encoding **f**ocal **a**dhesion **k**inase, FAK). Retrospective analysis of the DEGs also revealed differential expression of *PTK2* along with a series of other oncogenes and exhaustion-related genes (**Fig. 2b, c**). Consistent with our findings, CIBERSORT analysis revealed an association between immune cell infiltration levels and *PTK2* expression across many tumor types.[24] In particular, in colorectal adenocarcinoma (COAD), we observed a negative correlation between *PTK2* expression and $CD8^+$ T cell infiltration (**Extended Data Fig. 2a**). Additionally, correlation analysis between *PTK2* expression and exhaustion score revealed a clear positive correlation with $CD8^+$ T-cell exhaustion (**Extended Data Fig. 2b**).[25,26]

PTK2, a ubiquitously expressed nonreceptor tyrosine kinase, has been reported to be expressed in tumor cells, pericytes and fibroblasts.[27] However, in COAD, scRNA-seq analysis indicated *that PTK2 was predominantly expressed* in epithelial cells, particularly in stem-like epithelial cells (**Fig. 2d-g**). Moreover, *PTK2* was overexpressed in tumors, especially in the MMRp subtype (**Fig. 2h**). Immunohistochemistry (IHC) further confirmed hyperactivation of FAK signaling at the protein level in CRC tumors compared to adjacent normal tissue (**Fig. 2i**). Consistent with these findings, both the mRNA and protein levels of FAK were upregulated in tumors compared to normal tissues across multiple cancers, as evidenced by TIMER2 and the Human Protein Atlas database (**Extended Data Fig. 2c-g**).

To assess whether FAK activation was associated with T-cell exhaustion, we examined pFAK expression levels using DSP data and found a positive correlation between pFAK expression and immune checkpoint proteins (PD-1, TIM-3, and LAG-3) in the intratumoral region (**Fig. 2j**). This positive correlation was further validated using multiplex immunofluorescence (mIHC) staining. Cell classification and spatial distribution analysis of 45 regions of interest (ROIs) from the high and low pFAK expression groups in two sets of formalin-fixed paraffin-embedded (FFPE) sections revealed consistent findings (**Fig. 2k-l, Extended Data Fig. 3a-f**). Tumors with high pFAK expression exhibited a greater proportion of TIM-3^+ TILs than did those with low pFAK expression (**Fig. 2m, n**). Spatial analysis within 100 μm of $CK19^+pFAK^+$ tumor cells further supported these findings, revealing a greater proportion of TIM-3^+ TILs in tumors with high pFAK expression **(Fig. 2o, p).** Collectively, these data suggest that tumor-intrinsic FAK activation may play a critical role in driving T cell exhaustion.

Pharmacological inhibition of FAK leads to stable disease progression by reprogramming the TIME.

To investigate the impact of FAK inhibition on tumor progression and alterations in the TIME, we assessed the effects of the clinically available FAK inhibitor VS-4718 in murine colorectal tumor models, including MC38 (microsatellite instability, MSI) and CT26 (microsatellite stable, MSS) models. Compared with control mice, MC38 tumor-bearing mice treated with 50 mg/kg FAK inhibitor (FAKi) exhibited significantly reduced tumor growth and stable disease (**Fig. 3a**). This tumor-suppressive effect was consistently observed in the CT26 subcutaneous tumor model (**Fig. 3b**).

Subsequent scRNA-seq analysis of CT26 tumors allowed us to map the transcriptional landscape of the TIME. After quality control, we obtained transcriptomes from 47,442 cells and identified 13 main cell types, including various T/NK cell subsets, B cells, myeloid cells, endothelial cells, fibroblasts, and tumor cells, using the uniform manifold approximation and projection (UMAP) algorithm (**Fig. 3c, Extended Data Fig. 4a-i**). Notably, treatment with FAKi led to significant changes in T/NK cell clusters compared to those in controls (**Fig. 3d**). Differentially expressed gene analysis revealed that compared with control tumors, FAKi-treated tumors exhibited upregulated expression of cytotoxicity-associated genes (*Gzma*, *Ifngr1*, *Cxcl10*) and

downregulated expression of exhaustion-related genes (*Pdcd1, Lag3, Tox*) in $CD8^+$ T cells (**Fig. 3e, f**). Gene set enrichment analysis (GSEA) further indicated that FAKi treatment was associated with enhanced T cell differentiation and activation pathways (**Fig. 3g, h**). Given the reduction in $CD8^+$ T cells after FAKi treatment, we noticed that this reduction stemmed from the presence of a *Pdcd-1*^{high} $CD8^+$ T cell population (**Fig. 3i)**. Notably, analysis of $CD8^+$ T cell differentiation trajectories using Monocle 2 revealed distinct branches representing stem-like $CD8^+$ T cells (*Slamf6* and *Tcf7*), exhausted $CD8^+$ T cells (*Pdcd1 and Tox*), and proliferating $CD8^+$ T cells (*Birc5 and Top2a*) (**Fig. 3j, k**). FAKi treatment notably suppressed the exhaustion of stem-like $CD8^+$ T cells, maintaining them in a less differentiated state (**Fig. 3j-l**).

To explore changes in intercellular communication involving $CD8^+$ T cells, we analyzed the network of pathways associated with exhaustion (PD-L1 signaling) and cytotoxicity (TNF signaling). FAKi treatment was associated with reduced exhaustion pathway activity and enhanced cytotoxicity among $CD8^+$ T cells and other cell types (**Fig. 3m, n**). Validation through mIHC and flow cytometric analysis confirmed that FAKi treatment significantly reduced the proportion of terminally exhausted TIM-3^+PD-$1^+$$TOX^+$$CD8^+$ T cells (Tex cells) while increasing the percentage of stem-like $CD8^+$ T cells expressing TCF-1 in CT26 tumors (**Fig. 3o-r**). Furthermore, FAKi treatment increased the proportions of $GZMB^+$$CD8^+$ T cells (effector CTLs) and IFN$\gamma^+$$CD8^+$ T cells in both CT26 and MC38 tumors (**Fig. 3 s, Extended Data Fig. 5a-c**). Analysis of myeloid subsets also indicated a reduction in TIM-3^+ dendritic cells in FAKi-treated tumors, suggesting improved antigen-presenting cell (APC)-T cell interactions (**Extended Data Fig. 6a, b**). Together, these findings suggest that FAK inhibition suppresses tumor progression by preventing T cell exhaustion, maintaining a stem-like state, and enhancing T cell effector functions, thereby reshaping the tumor immune microenvironment toward an antitumor response.

Tumor-intrinsic FAK regulates TIL exhaustion in colorectal tumors

To investigate the role of tumor-intrinsic FAK in regulating the antitumor immune response, we utilized CRISPR-Cas9 gene editing to knock down *Ptk2* (encoding FAK) expression in CT26 tumor cells. Two single guide RNA sequences targeting *Ptk2* (sgPtk2) effectively reduced FAK protein expression without significantly impacting cell proliferation (**Fig. 4a, b**). Subsequently, we evaluated the impact of FAK knockdown on tumor growth in immunocompetent BALB/c

mice and immunodeficient BALB/c-nude mice. Strikingly, depletion of FAK resulted in a significant delay in tumor progression, especially in immunocompetent mice (**Fig. 4c, d**), suggesting an enhanced antitumor immune response upon FAK inhibition.

To dissect the cellular and molecular mechanisms underlying the regulation of the antitumor immune response by tumor-intrinsic FAK, we performed single-cell transcriptome analysis of sgPtk2 and control (Cas9) tumors. After stringent quality control, transcriptomes from 87,383 cells revealed 13 main cell types, with notable changes observed in T cell clusters in sgPtk2 tumors (**Fig. 4e-g, Extended Data Fig. 7a-h**). Differential expression analysis highlighted significant gene changes in $CD8^+$ T cells, macrophages, and monocytes within sgPtk2 tumors (**Extended Data Fig. 8a**). GSEA demonstrated enrichment of pathways related to lymphocyte differentiation and immune regulation in $CD8^+$ T cells from sgPtk2 tumors (**Extended Data Fig. 8b, c**). $CD8^+$ T cells from sgPtk2 tumors were enriched in genes related to T cell activation, lymphocyte proliferation and cytokine□cytokine receptor interactions (**Extended Data Fig. 8d**). Trajectory analysis revealed that FAK knockdown in tumor cells promoted the differentiation of $CD8^+$ T cells toward a proliferative state rather than an exhausted state (**Fig. 4h, Extended Data Fig. 8e, f**). Consistent with these findings, analysis of intercellular communication pathways revealed a reduction in the exhaustion pathway network (PD-L1 signaling) among $CD8^+$ T cells and other cells in sgPtk2 tumors compared to that in Cas9 tumors, suggesting a rescue from $CD8^+$ T cell exhaustion upon loss of tumor-intrinsic FAK (**Fig. 4i**). The reduction in $CD8^+$ T cell exhaustion in sgPtk2 tumors was further validated through mIHC analysis, revealing decreased PD-1^+TIM-3^+TOX$^+$$CD8^+$ T cells (exhausted T cells) and increased TCF-$1^+$$CD8^+$ T cells (stem-like T cells) compared to those in control tumors (**Extended Data Fig. 8g-i**). Spatial analysis of $CD8^+$ T cell exhaustion confirmed these findings, showing a significant decrease in exhausted T cells and an increase in functional $CD8^+$ T cells in the intratumoral area in sgPtk2 tumors (**Fig. 4j, k**). Furthermore, *in vitro* coculture experiments demonstrated that sorted $CD8^+$ T cells cocultured with sgPtk2 tumor cells exhibited reduced proportions of PD-1^+TIM-3^+TOX$^+$$CD8^+$ exhausted T cells and increased proportions of Ki67$^+$$CD8^+$ T cells, along with an expansion of TCF-1^+ stem-like T cells (**Fig. 4l-p**). In summary, these findings illustrate that tumor-intrinsic FAK plays a crucial role in regulating $CD8^+$ T cell exhaustion, highlighting its potential as a therapeutic target to enhance antitumor immunity in colorectal cancer.

Nuclear FAK promotes CD8$^+$ T-cell exhaustion by transcriptionally regulating the SP1-IL-6 axis

To investigate how tumor-intrinsic FAK regulates T cell exhaustion, we first examined whether FAK translocates to the nucleus and functions as a transcription factor (TF). mIHC and immunofluorescence staining revealed the nuclear localization of FAK protein in human CRC tumor cells and CT26 cells, which was confirmed by colocalization studies and western blot analysis (**Fig. 5a-d**). To uncover the potential mechanism of nuclear FAK-targeted genes, we performed cleavage under targets and tagmentation (CUT&Tag) in CT26 cells (**Fig. 5e**). Strikingly, approximately 54.71% of the total FAK binding peaks were located within ±1 kb of the TSSs of a total of 3,823 identified peaks (**Fig. 5f**). Pathway enrichment analysis revealed that FAK-binding genes were enriched in the cell cycle, cytokine, TGF-beta and interleukin-6 (IL-6) signaling pathways (**Extended Data Fig. 9a**). Further analysis revealed FAK-targeted transcription factors, including SP1 (specificity protein 1) (**Fig. 5g**). Specifically, increased binding was observed at the SP1 promoter region, as predicted by computational models (**Fig. 5h, i** and **Extended Data Fig. 9b**). Validation through CUT&Tag-qPCR confirmed reduced FAK enrichment at the SP1 promoter and decreased SP1 mRNA expression in FAK-knockdown (sgPtk2) cells compared to controls (**Fig. 5j, k**). Immunofluorescence staining confirmed decreased SP1 protein levels in sgPtk2 cells (**Fig. 5l**). Based on the findings that FAK-regulated transcription factors might be involved in inflammatory cytokine signaling pathways, we further validated cytokine/chemokine gene expression differences between cas9 and sgPtk2 cells. The results showed that the expression of *Il6*, *Csf1* and *Csf2* was significantly reduced and that the expression of *Cxcl10* was significantly increased in sgPtk2 cells. Strikingly, there was an approximately 10-fold decrease in the mRNA expression of the SP-1 target *Il6* in sgPtk2 cells compared to that in control cells (**Fig. 5m**).[28] All these data indicated that FAK could induce IL-6 production through SP1 transcriptional regulation.

To investigate the downstream effects of IL-6 on T cell exhaustion, splenic CD8$^+$ T cells were isolated and then exposed to IL-6 *in vitro*. The results showed that IL-6 significantly promoted the expression of the exhaustion genes *Pdcd1* and *Havcr2* in T cells, while the expression of the effector gene *Ifng* was suppressed by IL-6 (**Extended Data Fig. 10a, b**). We further confirmed that IL-6 promoted the expression of exhaustion markers, such as PD-1, TIM-3 and TOX, in

$CD8^+$ T cells and increased the proportion of exhausted $CD8^+$ T cells (PD-1^+TOX$^+$CD8$^+$ T cells, TIM-3^+TOX$^+$CD8$^+$ T cells and PD-1^+TIM-3^+TOX$^+$CD8$^+$ T cells) in a time-dependent manner (**Fig. 5n, o**). To verify the downstream mediators of IL-6-driven T cell exhaustion, we investigated the status of its downstream target, STAT3.[29] As expected, IL-6 promoted both the mRNA and protein expression of STAT3 in a time-dependent manner (**Extended Data Fig. 10c, d**).

To validate these results *in vivo*, we examined IL-6 mRNA expression in scRNA-seq data from both sgPtk2 tumors and cas9 tumors. As expected, there was a lower expression level of IL-6 mRNA in sgPtk2 tumors than in Cas9 tumors, and these results were confirmed by ELISA (**Extended Data Fig. 10e, f**). Next, we performed mIHC analysis of Cas9, pFAK, IL-6, CD8 and p-STAT3 in Cas9 and sgPtk2 tumors and found a significant reduction in the IL-6 protein in FAK-deficient tumors (**Fig. 5p-r**). More importantly, we observed a dramatic increase in the IL-6 protein in pFAK$^+$ tumor cells, suggesting that IL-6 is mainly secreted by FAK-activated tumor cells (**Fig. 5 s**). In addition, consistent with the *in vitro* results, p-STAT3 expression and the proportion of p-STAT3$^+$CD8$^+$ T cells were also significantly lower in sgPtk2-treated tumors than in control tumors (**Extended Data Fig. 10g-j**).

To further understand the mechanism by which FAK inhibition influences the TME, we performed GSEA. The GSEA results revealed that the DEGs associated with $CD8^+$ T cells were correlated with cytokines. Analysis of cell□cell communication revealed that the CXCL signaling pathway network was increased in $CD8^+$ T cells in tumors from FAKi-treated mice. In contrast, the CSF signaling pathway network was decreased in FAKi-treated tumors compared to control tumors (**Extended Data Fig. 11a-c**). Therefore, we further validated changes in cytokine secretion between FAKi-treated and control CT26 cells and found that FAKi significantly reduced the secretion of cytokines, including IL-6, involved in T cell recruitment and activation (**Extended Data Fig. 11d-f**). In conclusion, these results elucidate a mechanism by which nuclear FAK enhances T cell exhaustion through transcriptional regulation of the SP1-IL-6 axis in tumor cells, highlighting FAK as a potential therapeutic target for modulating immune responses in the tumor microenvironment.

FAK inhibitors potentiate immune checkpoint blockade (ICB) therapy *in vivo*.

Given that FAK inhibition suppresses tumor growth by reprogramming the tumor microenvironment, we aimed to further investigate its potential to improve immunotherapy efficacy. We found that FAKi synergized strikingly with immunotherapies when combined with low-dose 5-fluorouracil (20 mg/kg, i.p., '5-Fu[20]') in both CT26 (MSS) and MC38 (MSI) tumor models of human CRC, resulting in notable suppression of tumor growth compared with those treated with a FAK inhibitor or immunotherapy alone (**Fig. 6a, b**).

To decipher the underlying cellular and molecular mechanisms, we conducted scRNA-seq on tumor-infiltrating $CD45^+$ immune cells (**Fig. 6c**). After quality control, T-distributed stochastic neighbor embedding (t-SNE) analysis identified a total of 11 main cell types based on known expression markers (**Fig. 6d-e, Extended Data Fig. 12a-d**). Recluster analysis of $CD8^+$ T cells from four identified subsets revealed the following: precursor effector/memory $CD8^+$ T cells (Tpem) expressing stem-like markers (*Tcf7*, *Cd69* and *Mki67*) and effector/memory markers (*Ifngr1* and *Ccr2*); proliferating $CD8^+$ T cells (Tprolif) expressing proliferation markers (*Mki67*, *Bicr5* and *Top2a*); effector/memory $CD8^+$ T cells (Tem) expressing effector/memory markers (*Tnf*, *Ifngr1* and *Cd200*); and exhausted $CD8^+$ T cells (Tex) expressing exhaustion markers (*Tox*, *Havcr2* and *Pdcd1*) (**Fig. 6f, Extended Data Fig. 13a**). Notably, we observed significant expansion of Tpem clusters and Tem cell clusters in combination-treated tumors, whereas the proportions of Tex cells were dramatically lower in combination-treated tumors than in the other three groups (**Fig. 6g**). Furthermore, compared with those in the other three groups, $CD8^+$ T cells from combination-treated tumors exhibited reduced expression levels of exhaustion-related genes (*Havcr2*, *Pdcd1* and *Tox*) and increased expression levels of cytotoxicity-related genes (*Cd69*, *Ifngr1* and *Tnf*) (**Fig. 6h**).

Next, we computationally imputed pseudotime trajectories by utilizing Tpem cells as the root population, and Tpem cells differentiated toward two different trajectories (the Tem cell branch and Tex cell branch) through Tprolif cells, consequently forming a cytotoxic $CD8^+$ T lineage and an exhausted $CD8^+$ T lineage (**Fig. 6i**). We observed that there were significantly lower levels of exhaustion marker genes in the cytotoxic $CD8^+$ T lineage from the combination-treated tumors than in the other three groups. In contrast, the expression of cytotoxic marker genes was

significantly greater in $CD8^+$ T cells from the combination-treated group than in those from the other three groups (**Fig. 6j** and **Extended Data Fig. 13b**). We used GSEA to determine the pathways involved in $CD8^+$ T cells among the combination group and three other groups. As expected, $CD8^+$ T cells from combination-treated tumors were enriched in various pathways related to T-cell activities, including lymphocyte migration, proliferation, activation and interferon-beta production (**Fig. 6k**). The results of intercellular communication among $CD8^+$ T cells and other immune subsets revealed that combination treatment led to the loss of PD-L2 signaling, coupled with an increase in TNF signaling in $CD8^+$ T cells (**Extended Data Fig. 13c, d**).

To validate the findings from the scRNA-seq data, we carried out mIHC and flow cytometry to profile the $CD8^+$ T cell status in both CT26 and MC38 tumors. We confirmed that there was a significant decrease in IL-6 protein expression in the combination-treated group as well as in the FAKi alone group (**Extended Data Fig. 13e, f)**. We also detected a significant reduction in $pSTAT3^+CD8^+$ T cells and $TOX^+TIM\text{-}3^+CD8^+$ T cells in the combination and FAKi groups (**Fig. 6l-n**). We further confirmed that there was a significant increase in the proportion of $CD8^+$ T cells exhibiting an effector phenotype ($CD44^+$ $CD62L^-$) in tumors from combination-treated mice compared with those from the other three groups (**Extended Data Fig. 13g**). More importantly, combination treatment also augmented the production of cytolytic granules (GZMBs) and cytokines (IFNγ) in tumor-infiltrating $CD8^+$ T cells (**Extended Data Fig. 13h**). Taken together, these findings demonstrate that inhibition of FAK enhances checkpoint therapy across CRC models by potentiating tumor-resident $CD8^+$ T cell functionality and cytotoxicity and reinvigorating exhausted states through suppression of the SP1-IL-6 proinflammatory axis (**Fig. 6o**).

DISCUSSION

This work demonstrated that the dysregulation of FAK signaling was associated with the heterogeneity and exhaustion of $CD8^+$ T cells within the spatial context of the tumor microenvironment and strongly correlated with patient survival in CRC patients. Importantly, our findings provide proof of concept that targeting FAK using small molecule inhibitors

enhances the efficacy of αPD-1 and αTIM-3 immunotherapies by bolstering cytotoxicity among tumor-resident $CD8^+$ T cells and reversing exhausted states in mouse models of CRC. Mechanistically, we elucidated that nuclear FAK orchestrates SP1/IL-6-mediated T cell exhaustion and governs the transcriptional regulation of proinflammatory cytokines and chemokines.

In solid tumors such as CRC, the infiltration of T cells into tumor beds has long been associated with favorable outcomes.[30,31] However, little is known about how the spatial immune microenvironment impacts cancer and whether it plays a role in regulating the TIL exhaustion status and the efficacy of immunotherapies in the tumor suppressive microenvironment.[32] Moreover, the mediators contributing to immune suppression and the limited response to immunotherapy in patients with colorectal cancer remain unexplored. Our previous work and others have shown that targeting FAK in pancreatic cancer cells reduces the number of tumor-promoting macrophages and MDSCs and improves the response to anti-PD1/CTLA4 checkpoint therapy.[33,34] In this work, we demonstrate that FAK contributes to spatial immune suppression and T cell exhaustion in human colorectal cancers by integrating digital spatial analysis and scRNA-seq datasets. FAK inhibition could reprogram the immune microenvironment and reinvigorate the exhausted state, and FAK inhibitor treatment reduced the number of terminally exhausted $PD1^+TIM\text{-}3^+CD8^+$ T cells, resulting in slowed tumor progression in mouse models of human CRC.

The exhausted state of T cells is characterized by an overactive immune checkpoint response, which is regulated by the expression of inhibitory receptors such as PD-1, LAG-3, TIM-3, CTLA-4, and PD-1; in particular, this response has received much attention in the field of immuno-oncology due to its central role in regulating T cell function and its correlation with disease progression and treatment responses in various cancers.[14,16,35,36] Targeting PD-1 with checkpoint inhibitors, such as nivolumab and pembrolizumab, has been shown to be effective in reversing T cell exhaustion and restoring antitumor responses, leading to clinical benefits in some cancer patients.[37,38] However, while targeting PD-1 has shown promising results in some cancers, a significant proportion of patients still do not respond to this treatment,[39,40] highlighting the need for additional therapeutic targets and a better understanding of the complex mechanisms

underlying T-cell exhaustion in cancer. T-cell immunoglobulin and mucin-domain-containing protein 3 (TIM-3) is considered an immune checkpoint molecule similar to PD-1 and CTLA-4.[41,42] Studies have highlighted the role of TIM-3 expression on $CD8^+$ T cells in relation to disease stage in human colorectal cancer (CRC), as well as the potential benefits of TIM-3 blockade in enhancing antitumor responses.[43,44] Despite the promising preclinical data, most clinical trials targeting TIM-3 with monoclonal antibodies in cancer have not met their primary endpoints or shown significant clinical benefits.[45,46] These outcomes highlight the complexity of cancer immunotherapy and the need for multifaceted treatment approaches. Studies have shown that long-term persistence of $TCF1^+$ stem-like T cells is important for achieving durable responses to immunotherapies, such as checkpoint inhibitors.[47–49] In this work, we demonstrated that hyperactivation of FAK in tumor cells is a key contributor to $CD8^+$ T cell exhaustion and immune suppression within the tumor microenvironment. More importantly, pharmacological targeting or genetic loss of FAK dramatically reduces TIM-3 expression on $CD8^+$ T cells, pushing T cells toward a cytotoxic state with proliferative and functional capacities.

FAK is well known as a nonreceptor protein tyrosine kinase that clusters at focal adhesion structures and plays a role in regulating cell adhesion, migration and survival. David Schlaepfer reported that FAK translocated to the nucleus and defined a scaffolding role for nuclear FAK in facilitating cell survival.[50] Recently, Margaret Frame demonstrated that nuclear FAK is associated with chromatin and interacts with TFs to control evasion of antitumor immunity.[51] Consistent with these reports, we also observed that FAK is located in the cell nucleus in the context of colorectal cancer. We speculate that FAK might function directly as a core transcriptional machinery. Strikingly, CUT&Tag analysis revealed that approximately 54.71% of the total FAK binding peaks were located within ±1 kb of the TSSs of a total of 3,823 identified peaks, confirming that FAK functions as a transcription factor (TF). More importantly, consistent with the binding sites predicted for FAK by AlphaFold3,[52] we identified SP1 as a direct target of nuclear FAK. We propose a model in which nuclear FAK binds to the promoter of SP1, which induces SP1 transcription and thereby leads to an increase in the production of IL-6, a direct target of SP1.[28] Indeed, we demonstrated that IL-6 was a key contributor to T cell exhaustion through the activation of STAT3 both *in vitro* and *in vivo*. We also observed that there was a significant increase in the number of NK cells upon inhibition of FAK, suggesting

that loss of FAK might enhance the tumor-killing ability of NK cells. The detailed underlying mechanisms warrant further exploration.

Combining FAK inhibitors with ICB therapy represents a strategy for anticancer therapy.[53,54] Our previous work demonstrated that a combination of FAK inhibitors and anti-PD-1/CTA4 antibodies reduced the number of immunosuppressive cells and improved overall survival in mouse models of human pancreatic cancer.[33] Consistent with previous reports,[51] here, we found that targeted inhibition of FAK dramatically improved the efficacy of anti-PD1/TIM-3 checkpoint therapy in both MSS and MSI mouse models of human CRC as a result of reinvigorating exhausted states of tumor-infiltrating lymphocytes and potentiating effector T cell cytotoxicity. Taken together, the results of these studies provide promising evidence that targeting the FAK pathway may represent a promising strategy for cancer immunotherapy.

In summary, our data demonstrate the importance of the spatial status of infiltrating immune cells in human colorectal cancer patients, with an emphasis on spatial profiling of $CD8^+$ TILs in the tumor microenvironment. These results highlight the importance of considering the spatial distribution of immune cells and the underlying mechanisms of immune exhaustion in the design of cancer immunotherapies. We found that nuclear FAK functions as a core transcriptional machinery to aggravate $CD8^+$ T cell exhaustion by regulating the SP1-IL-6 axis in CRC. These insights provide a compelling rationale for targeting FAK to enhance the effectiveness of immunotherapy in CRC and advocate for future investigations into spatially nuanced immunotherapeutic strategies.

METHODS

Human tumor specimen collection

Human colorectal cancer specimens were collected from patients with histologically confirmed colorectal cancer who underwent curatively surgical resection at the Department of Gastrointestinal Surgery, West China Hospital, Sichuan University, China. This project was approved by the West China Hospital Medical Committee approval (2020-374). The clinical and

pathological parameters of the included patients were obtained from the patient's electronic medical records (**Supplemental Table 6**).

Digital spatial profiling (DSP)

NanoString's GeoMx digital spatial profiling (DSP) was used for multiplexed and spatially resolved profiling analysis of pretreated tumor samples. The FFPE tissue slides were stained with a Texas red-labeled CD45 antibody (NanoString Technologies, US), Alexa Fluor 532-labeled PanCK, and SYTO13 to facilitate the identification of tissue morphology, and the regions of interest (ROIs) were defined according to these morphological marker antibodies. Then, the FFPE tissue slides were incubated with unique oligonucleotide-labeled antibodies, including the immune cell profiling core panel and the IO drug target module panel, which are described in detail in **Supplemental Table 1**. The stained slides were loaded onto a GeoMx instrument and scanned. The information contained in the collected ROI was analyzed by an nCounter Analyzer (NanoString Technologies, US) and then returned to the DSP system for data analysis and visualization.

Digital spatial profiling (DSP) was performed on the 10 tissue samples, applying 2 panels (immune cell panel and IO drug target panel, **Supplemental Table 2**), to demonstrate the proteomic characteristics of colorectal cancer. The DSP workflow is shown in **Extended Data Fig. 1a**. Then, 116 circular regions of interest (ROIs) were selected from 10 tissue slices and divided into intratumoral (%PanCK$^+$ area>95%), proximal (5%<%PanCK$^+$ area <95%) and distal (%PanCK$^+$ area <5%) regions based on their histological features (**Extended Data Fig. 1b**).

Immunohistochemical staining

All involved tissue samples were processed into paraffin. Paraffin-embedded tissues were cut at 5 μm and stained for immunohistochemistry. Slides were immersed in antigen retrieval buffer (Gene Tech, China) at a 1:500 dilution in distilled water. Antigen retrieval was then performed in a microwave oven for ∼20 min. Then, 2% BSA (BioFroxx, Germany) was used for blocking for 10 min, and the primary antibody (details of the antibodies are described in **Supplemental Table 3**) was diluted in PBS containing 1% BSA and applied overnight. A secondary antibody (Thermo

Fisher Scientific, US) was added after washing the slides for 30 min. After washing, DAB solution (Gene Tech, China) was added for coloring.

Immunofluorescence staining

FAK and SP1 expression and location were analyzed in CT26 cells. A total of 5×10^4 cells were seeded in confocal dishes in DMEM supplemented with 10% FBS. After cell adherence, the medium was replaced with DMEM supplemented with 1% FBS, and the cells were starved for 12 h. Immunofluorescence staining was performed according to standard procedures. Rabbit anti-FAK antibody and rabbit anti-SP1 antibody were used as the primary antibodies (details of the antibodies are described in **Supplemental Table 3)**, and the secondary antibody was an AF555-labeled goat anti-rabbit IgG (H + L) antibody (Invitrogen, US). The fluorescence was imaged using a laser confocal microscope (Leica-STELLARIS, Germany) and quantified using ImageJ.

Multiplex immunohistochemistry (IHC)

Multiplex IHC staining was performed using an Opal 7-color kit (Akoya Bioscience, US). Briefly, the sections were dewaxed with xylene for 20 minutes. Then, ethanol was used for rehydration. Microwave treatment was performed for antigen retrieval with antigen retrieval buffer. Next, all sections were cooled at room temperature for 30 minutes. Endogenous peroxidase activity was blocked using Antibody Diluent/Block (Akoya Bioscience, US) for 10 minutes at room temperature. The slides were then incubated for 1 hour at room temperature with the primary antibody (details of the antibodies are described in **Supplemental Table 3**), for 20 minutes at 37°C with the secondary reagents, and for 10 minutes at room temperature with Opal working buffer. The above procedures were repeated for other antibodies, and the antibodies were removed by microwave treatment before another round of staining was performed. Nuclear staining was performed using DAPI (Akoya Bioscience, US) for 5 minutes at room temperature. Slides were scanned at 20× magnification using the Vectra Polaris system (Akoya Biosciences, US). Whole-tissue scans were analyzed with Qupath software (https://qupath.github.io) using area quantification and a cytonuclear module.[55]

Image analysis

The slides were visualized using the Vectra Polaris system (Akoya Biosciences, US), and a multispectral image of the whole slide was scanned using a 20× objective lens. Multispectral image unmixing was performed using QuPath software (version 3.0).[55] Briefly, the DAPI-positive cells were identified by the "cell detection" command, and each single channel intensity threshold was selected using "Object classification." We determined the number of positive cells with the "Load classifier" and counted the areal proportions by dividing the channel-positive cell counts by all the cells detected as DAPI positive. Then, all detected cells were divided into different subgroups for further analysis, and defective TMA cores or areas with ruptured or folded tissue were reanalyzed or excluded. Spatial distance is calculated by "distance to centroid distances 2D". All other multispectral image unmixing methods were performed using HALO software. Image analysis algorithms were built using the Indica Labs High-Plex FL v2.0 module to perform DAPI-based nuclear segmentation and detect fluorescence-positive cells by setting a dye cytoplasm positive threshold. The spatial analysis module was used for proximity analysis, infiltration analysis and density analysis.

Cell proliferation

For CT26_cas9 and CT26_sgPtk2 cells, 2000 cells per well were seeded into 96-well plates in DMEM supplemented with 10% FBS. After 3 days and 6 days, CCK-8 solution (Life-ilab, China) was added to each well, and the plates were then incubated at 37°C. After 2 h, the absorbance at 450 nm was measured using a microplate reader (Thermo Fisher Scientific, US).

Western blot

Cells were lysed in RIPA lysis and extraction buffer (Thermo Fisher Scientific, USA). The protein concentration was assessed using the BCA Protein Assay Kit (Life-ilab, China). Proteins were loaded into each lane of a polyacrylamide gel. After electrophoretic separation, the proteins were transferred to a PVDF membrane (Sigma□Aldrich, Germany). The membranes were blocked for 1 h in Tris-buffered saline containing 0.05% Tween 20 (TBS) and 5% nonfat dry milk. Then, the cells were incubated with a primary antibody (the details of the antibodies used are described in **Supplemental Table 3**) at 4°C overnight. The membranes were washed 3 times with TBS for 5 minutes each and then incubated with a secondary antibody (Thermo Fisher

Scientific, US). An enhanced chemiluminescence (ECL) detection system (Tanon 5500, China) was used to image specific blots.

Generation of stable cell lines

Crispr-Cas9 genome editing technology was used to knock down Ptk2 gene expression in CT26 cells. The sequences for sgPtk2_1 and sgPtk2_2 were as follows: sgPtk2_1 F: CACCGGTGCACCTCCTCCGATCGC; sgPtk2_1 R: AAACGCGATCGGAGGAGGTGCACC; sgPtk2_2 F: CACCGTCGAGTACTAAGACTCACC; and sgPtk2_2 R: AAACGGTGAGTCTTAGTACTCGAC.

The annealed sgPtk2_1 and sgPtk2_2 were cloned and inserted into the BsmBI restriction sites of the V2TC plasmid to construct the transfer plasmids used for lentiviral packaging. Then, the 293T cells were transfected with the packaging plasmids pMD2. G, psPAX2, and the transfer plasmid using the calcium phosphate transfection method. The quantities of packaging plasmids used for the 6-well plates were pMD2. G, 1 μg; psPAX2, 2 μg; and shuttle plasmid, 4 μg. At 36 and 48 hours posttransfection, the culture supernatants were collected and filtered through a 0.45 μm filter to harvest the lentiviral particles.

CT26 cells were infected with Lenti-V2T to generate a Cas9-expressing CT26 cell line. The cells were selected using DMEM containing 10% FBS, 1% penicillin□streptomycin, and 8 μg/μL puromycin for one week. The resulting cell line stably expressing the Cas9 protein was termed CT26-Cas9. To obtain the FAK-knockdown CT26 cell line, CT26-Cas9 cells were infected with Lenti-V2TC-Ptk2-gRNA, which expresses both sgPtk2 and mCherry, and then cells positive for mCherry expression were sorted. The knockdown efficiency of FAK in the CT26 cell line was validated using a T7 endonuclease assay and Western blot analysis.

Isolation and activation of $CD8^+$ T cells

The spleens of C57BL/6 mice were dissected and grinded with a syringe plunger, followed by filtration with a 40 μm cell filter and treatment with 1x RBC lysis buffer (Invitrogen, USA). The cells were collected by centrifugation at 1500 rpm for 5 min, and the naïve T cells were harvested using a MojoSort™ mouse $CD8^+$ T cell isolation kit (#480008, Biolegend, US) following the manufacturer's instructions. For $CD8^+$ T cell activation, 24-well flat-bottom plates

were coated with 1.5 μg/mL of anti-CD3 (#BE0001, BioXcell, US) and anti-CD28 (#BE0015, BioXcell, US) antibodies and incubated at 4°C overnight. The wells were subsequently washed with PBS, after which 5×10^5 T cells were seeded and cultured at 37°C with 5% CO_2 in RPMI-1640 medium (HyClone, US) supplemented with 10% heat-inactivated fetal calf serum (ZETA LIFE, US), 1% penicillin and streptomycin (Gibco, US), 1% nonessential amino acids (Gibco, US), 1% sodium pyruvate (Gibco, US), 2% HEPES (Gibco, US), and 10 ng/mL IL-2 (#AF-212-12, PeproTech, US) for 24 h.

In an IL-6-induced Stat3 phosphorylation T cell assay, T cells were activated in the presence or absence of recombinant mouse IL-6 (5, 10, 50, 100 ng/mL, #AF-216-16, PeproTech, US) for 0, 5, 10, 30, or 60 min, and p-Stat3 expression was assessed by western blot analysis.
In the IL-6-induced exhaustion of T cells assay, T cells were activated in the presence or absence of recombinant mouse IL-6 (10 ng/mL) for 3 days or 6 days, whereas exhaustion markers were assessed by qPCR and flow cytometric analysis.

Tumor-CD8$^+$ T cell coculture system

Unless otherwise stated, CT26_cas9 and CT26_sgPtk2 cells were seeded at a 1:5 ratio (tumor cell:CD8$^+$ T cell) into a 24-well plate. Activated T cells (5×10^5 cells/well) were added to plates containing tumor cells. After approximately 6 days, all cells were collected and analyzed by flow cytometry.

Enzyme-linked immunosorbent assay (ELISA)

ELISA was carried out using a mouse IL-6 ELISA kit (#VAL604G, Novusbio, US) according to the manufacturer's instructions. Tissues were disrupted using a Bullet Blender Tissue Homogenizer (Next Advance, US) and lysed in RIPA lysis and extraction buffer (Thermo Fisher Scientific, US). The protein concentration was assessed using the BCA Protein Assay Kit (Life-ilab, China) to normalize the ELISA results.

Animal models

The CT26 cells and MC38 cells were maintained at 37°C with 5% CO_2 in RPMI-1640 medium (HyClone, US) supplemented with 10% heat-inactivated fetal calf serum (ZETA LIFE, US),

penicillin (Gibco, US), and streptomycin (Gibco, US). In all animal experiments, the mycoplasma detection results for all cell lines were negative. Six- to eight-week-old female C57BL/6, BALB/C and BALB/C nude mice were used for the subcutaneous tumor mouse models. Briefly, 2.5×10^5 CT26 cells and 5×10^5 MCA205 cells in 50 μL of Matrigel (Corning, US) were injected subcutaneously into each mouse's right back. Tumor volume (length × (width^2)/2) was assessed by caliper measurements every other day, and cohorts of mice were randomized into different treatment groups according to tumor volume. All animal studies were approved by the West China Hospital Animal Ethics Committee (2020361A)

Inhibitors and neutralizing antibodies

FAKi was purchased from Selleck, Inc. (#S7685, US). VS-4718 was dissolved in DMSO for *in vitro* study. For animal experiments, 50 mg/kg of VS-4718 was dissolved in vehicle (0.5% carboxymethyl cellulose (Sigma Aldrich, Germany) and 0.1% Tween-80 (Sigma Aldrich, Germany) in sterile water) and administered orally by gavage every 12 hours. 5-Fu (#HY90006, MCE, USA) was dissolved in PBS and administered by intraperitoneal (i.p.) injection every 2 days at 20 mg/kg. Monoclonal anti-TIM-3 antibodies (#BE0115, BioXCell, US) and anti-PD-1 antibodies (#BE0146, BioXCell, US) were given by intraperitoneal (i.p.) injection every 4 days at 10 mg/kg. Isotype controls (#BE0089, BioXCell, US) were used at the same concentration in control mice.

CUT&Tag

The CUT&Tag assay was conducted following the manufacturer's protocol (#HD101, Vazyme, China). Briefly, Concanavalin A-coated magnetic beads were incubated with CT26_cas9 or CT26_cas9_sgPtk2 cells at room temperature for 10 min, and anti-FAK antibody (1:50, #3285s, CST, US) was added and rotated at 4°C for 12 h. The samples were washed 3 times and then incubated with a secondary antibody (goat anti-rabbit IgG H&L, #AB206-01-AA, Vazyme, China) at 37°C for 30 min. After washing, the samples were incubated with Hyperactive pA/G-Transposon Pro and fragmented with $MgCl_2$. The fragmented DNA was extracted from the samples and amplified by PCR. Libraries were constructed using the TruePrep Index Kit V2 for Illumina (#TD202, Vazyme, China) and sequenced on an Illumina NovaSeq platform, and 150-bp paired-end reads were generated.

For CUT&Tag-qPCR, DNA samples were obtained according to the Hyperactive Universal CUT&Tag Assay Kit (#TD904, Vazyme, China), in which the target DNA fragments with DNA spike-in as a standard reference fragmented by pA/G-Tn5 were specifically recovered for qPCR to quantify the abundance of the target gene.

Flow cytometry

Single-cell suspensions of the tumors were obtained by incubating minced tissues with 3 mg/mL collagenase A (Roche, Germany) and 1 mg/mL DNase I (Roche, Germany) in RPMI 1640 medium at 37°C for 30 min. The resulting cell suspensions were passed through a 40 μM cell filter and treated with 1× RBC lysis buffer (Invitrogen, USA). Finally, the suspension was washed with PBS, and the cells were counted for flow cytometric analyses. First, the cells were incubated with Fixable Viability Stain 700 to gate viable cells. Then, the cells were washed with flow cytometry staining buffer (PBS containing 2% BSA), and the Fc receptor (FcR) was blocked with TruStain FcX™ (anti-mouse CD16/32) antibody (BioLegend, US). The cells were incubated with cell surface antibodies for 30 min at 4°C. The cells were then washed twice with flow cytometry staining buffer. For intracellular staining, the cells were cultured in fixation buffer at 4°C for 45 min (eBioscience, USA). The cells were then washed twice with permeabilization buffer (eBioscience, US). The cells were incubated with the appropriate intracellular antibodies for an additional 30 min at 4°C. The details of the antibodies used are described in **Supplemental Table 4**. The cells were then washed twice with permeabilization buffer and resuspended in flow cytometry staining buffer.

RT□qPCR

RNA was prepared according to the TRIzol reagent (Invitrogen, US) protocol. After the generation of complementary DNA, qPCR with reverse transcription was performed as described previously, and all expression levels were normalized to those of an internal housekeeping gene (*Gapdh*). The primers used are listed in **Supplemental Table 5**.

Protein arrays

CT26 cells were stimulated overnight with FAKi (1 μM) or DMSO (Sigma Aldrich, Germany). The cell supernatants were then collected after centrifugation. Cytokines in the cell supernatants were then analyzed with the Proteome Profiler Mouse Cytokine Array Kit A (#ARY006, R&D Systems, US). The blots were visualized with chemiluminescence using a detection system (Tanon 5500, China) and quantified using ImageJ.

Isolation of CD45$^+$ cells for scRNA-seq

Single−cell suspensions of the tumors were obtained by incubating minced tissues with 3 mg/mL collagenase A (Roche, Germany) and 1 mg/mL DNase I (Roche, Germany) in RPMI 1640 medium at 37°C for 30 min. The resulting cell suspensions were passed through a 40 μM cell filter and treated with 1× RBC lysis buffer (Invitrogen, USA). Finally, the suspension was washed with PBS and counted for isolation. Then, the Fc receptor (FcR) in the cells was blocked with a TruStain FcX™ (anti-mouse CD16/32) antibody (#101319, BioLegend, US). After blockade, the cells were incubated with a PE-conjugated anti-mouse CD45 antibody (#103106, BioLegend, US) for 20 min at 4°C. After washing, anti-PE MicroBeads (#130-048-801, Miltenyi, Germany) were added, and the mixture was mixed well and refrigerated for 15 minutes. After washing, the cell suspension was applied to the column, and labeled CD45$^+$ cells were collected for analysis.

Associations between *PTK2* expression and immune status

CIBERSORT (https://cibersort.stanford.edu/) was used to calculate the proportions of 20 types of immune cells via a cancer relative score, which allows for the prediction of the immune cell phenotype.

Analysis of *PTK2* expression

PTK2 expression was assessed in both tumor and normal tissues utilizing TIMER2, which can be accessed at http://timer.cistrome.org/.[26]

Differences in PTK2 protein expression were also investigated using the HPA database. We acquired and examined immunohistochemical (IHC) images of PTK2 protein expression in 4 tumor types. The HPA database is accessible through the website https://www.proteinatlas.org/.

Bioinformatics

Cut&Tag data preprocessing.

CUT&Tag data processing and analysis were performed following a standard protocol (https://yezhengstat.github.io/CUTTag_tutorial/index.html). The raw Cut-Tag reads were trimmed and filtered for quality using Trimmomatic (v. 0.39).[56] Paired-end reads were aligned [57]against mm10 genomes and spike-in sequences from *E. coli* genomes using Bowtie2 (v.2.5.1) with the parameters --local --very-sensitive-local --no-mixed --no-discordant --phred33 -I 10 -X 700 -p 15. Aligned reads were sorted, and nonuniquely mapped reads were marked using Picard (v.3.0.0) (http://broadinstitute.github.io/picard/). PCR duplicates and reads of low mapping quality (MAPQ < 10) were filtered using SAMtools (v.1.18).[58] We then identified peaks using MACS2 (v.2.2.7.1), [59] employing parameters with preprocessed bamfiles as follows: -t pathway of the two FAK antibody group bamfiles -c pathway of the two control group bamfiles -f BAMPE -g mm -B -p 0.01. Peaks were annotated using the R package ChIPseeker (v1.24.0).[60] The enrichment of gene ontology terms in sets of peaks was calculated using ClusterProfiler (v4.9.0.002).[61]

Peak heatmaps and genome coverage plots

To visualize CUT&Tag data coverage across the genome within protein-coding genes, read counts were normalized to the corresponding total reads aligned to the spike-in genome (*E. coli*). Normalized bigwigs were generated with the bamCoverage function from deepTools (v3.5.4).[62] The heatmaps were generated with the indicated regions (TSSs ± 3000 bp) with the computeMatrix function followed by the plotHeatmap functions of deepTools. Candidate gene coverage plots were generated using pyGenomeTracks (v3.8).[63]

Single-cell transcriptomic analysis

Library preparation and sequencing

The scRNA-seq libraries described in this study were generated utilizing the DNBelab C4 system. Initially, a suspension of single cells was processed through several stages, including droplet encapsulation, emulsification, and fragmentation. This was followed by the collection of mRNA capture beads, reverse transcription, cDNA amplification, and subsequent purification. According to the manufacturer's protocol, an indexed sequencing library was then assembled.

The concentration of the sequencing library was determined using the Qubit ssDNA Assay Kit (Thermo Fisher, US). Sequencing was performed on the DIPSEQ T1 platform at the National Gene Bank (CNGB, BGI-SHENZHEN, China). For data processing, the raw FASTQ files were analyzed using DNBelab_C4scRNA (v1.0.1) software (available at https://github.com/MGI-tech-bioinformatics/DNBelab_C_Series_scRNA-analysissoftware) and converted into a format compatible with Cell Ranger.[64]

Alignment and quantification

The sequencing data were processed using STAR software (v2.5.3) [57] with default parameters and mapped to the mm10 reference genome. The aligned reads were subsequently screened to identify valid cell barcodes and unique molecular identifiers (UMIs), which facilitated the creation of a gene-cell matrix for further analysis.

Quantity of scRNA-seq data

The gene-cell matrix was loaded by the Read10X function of the R package Seurat (v4.1.1).[65] Genes expressed in fewer than 3 cells were identified. Additionally, cells were filtered based on four standards: UMIs, the number of genes, the percentage of mitochondrial (Mt) genes, and the percentage of ribosomal protein large/small (Rpl/s) genes. The percentage of Mt/Rpl/s genes was calculated by the PercentageFeatureSet function. These filtering standards vary across different datasets and depend on the data characteristics. In the FAK inhibitor and FAK KO experiments, cells were removed if they had UMIs less than 1100 or greater than 60000, number of genes less than 700 or greater than 7500, Mt gene percentage greater than 15%, or Rpl/s gene percentage greater than 30% (Fig S4, S7). Similarly, in the therapeutic experiments, cells were excluded if they had UMIs less than 1000 or greater than 17000, number of genes less than 900 or greater than 4700, Mt gene percentage greater than 10%, or Rpl/s percentage greater than 30% (**Extended Data Fig. 12**). Additionally, only $CD45^+$ cells were retained in the therapeutic group samples. Following quality control, the analysis included 47,442 single cells from FAKi experiments, 87,383 from FAK KO experiments, and 75,631 from therapeutic experiments for downstream analysis.

Dimensionality reduction and cell type classification

After quality control of the cells and genes, dimensionality reduction and unsupervised clustering were performed by the R package Seurat (v4.1.1).[65] To address batch effects, each sample was individually processed using the NormalizeData and FindVariableGenes functions. Subsequently, batch integration was achieved through the FindIntegrationAnchors and IntegrateData functions, setting the dims parameter to 50. This integrated dataset was then scaled for principal component analysis, utilizing the first 20 principal components to construct a shared nearest neighbor (SNN) network. The Louvain algorithm was employed to identify cell clusters, with resolution settings adjusted according to the specific characteristics of each dataset. Visualization of these clusters in two-dimensional space was accomplished using either UMAP or t-SNE, implemented via the RunUMAP or RunTSNE functions, respectively. Markers for each cluster were detected using the FindAllMarkers function in Seurat with the following parameters: min.pct = 0.1, logfc.threshold = 0.25, pseudocount.use = 0.1, only.pos = T. To annotate each cluster as a specific cell type, we selected some classic markers of immune cells, epithelial cells and fibroblasts. The cell types were annotated using a violin or dot diagram.

Single-cell level differentially expressed gene (DEG) analysis

Differential gene expression analysis was conducted using the FindMarkers function from the Seurat R package. For this analysis, the cell populations of interest were specified as ident.1 and ident.2. We calculated the fold changes in the mean gene expression levels between these populations. Only genes that exhibited a Bonferroni-adjusted P value of less than 0.05 and an absolute log2-fold change greater than 0.25 were selected for subsequent analysis.

Discriminate between malignant and nonmalignant cells

Single-CEll Variational ANeuploidy Analysis (SCEVAN) is a rapid variational algorithm designed for deconvoluting the clonal substructure of tumors using single-cell RNA-seq data[66] that can automatically and accurately discriminate between malignant and nonmalignant cells. The R package SCEVAN is user-friendly, and the pipelineCNA function can perform almost all analyses when provided with a raw gene-cell matrix.

Monocle2 pseudotime trajectory inference

We constructed the single-cell trajectory of $CD8^+$ T cells by using a reversed graph embedding method implemented by the R package Monocle2 (v. 2.16.0)[65] in the FAK inhibitor and FAK KO experiments. The raw gene-cell matrix of $CD8^+$ T cells was extracted by the GetAssayData function of Seurat. Then, we integrated the expression matrix of CD8 T cells from each sample using the newCellDataSet function of Monocle2. After this, the expression matrix was normalized by the estimateSizeFactors and estimateDispersions functions of Monocle2. The top 900 highly expressed genes identified by the FindVariableFeatures function of Seurat were used to order cells in Monocle to construct a CD8+ T-cell DDRtree trajectory plot using the setOrderingFilter and reduceDimension functions of Monocle2. The signature of each state was calculated based on genes that were differentially expressed among the other states. States were annotated as stem-like CD8 T cells (*Slam6f*, *Tcf7*), proliferating CD8 T cells (*Birc5*, *Top2a*), or exhausted CD8 T cells (*Pdcd1*, *Tox*).

Slingshot pseudotime trajectory inference

We used Slingshot (v1.6.0)[67] to construct cell trajectories to discover cell-state transitions in CD8+ T cells in therapeutic experiments. CD8 T cells were annotated as CD8_Tpem (*Tcf7*, *Cd69*, *Mki67*, *Ifngr1*, *Ccr2*), CD8_Tprolif (*Mki67*, *Bicr5*, *Top2a*), CD8_Tem (*Tnf*, *Ifngr1*, *Ccr7*, *Cd200*, *Tnfrsf4*, *Tnfrsf18*), and CD8_Tex (*Tox*, *Havcr2*, *Pdcd1*, *Tigit*, *Entpd1*) (**Fig. 6f, Fig. S13a**). We selected CD8_Tem cells as the root state when calculating the trajectories and pseudotime using the slingshot function of the R package Slingshot (v1.6.0).[67] $CD8^+$ T cells were split into two lineages: cytotoxic and exhausted trajectories. The results were visualized using the R package ggplot2 (v3.4.4) (https://github.com/tidyverse/ggplot2/).

Construction of the cell□cell communication network

Intercellular communication networks were constructed and visualized using the CellChat R package (version 2.1.2)[68] (https://github.com/jinworks/CellChat?tab=readme-ov-file). The CellChat database for mice, which encompasses 2,377 cell□cell communication interactions across three categories—Secreted Signaling, ECM-Receptor, and Cell□Cell Contact—was used. The downstream analysis included inferring the cell□cell communication probability using the computeCommunProb and filterCommunication functions. The communication probabilities at both the signaling pathway and gene levels were calculated by the computeCommunProb and

computeCommunProbPathway functions. All the results were integrated by the aggregateNet function. Significant signaling pathways were visualized as circle plots using the netVisual_individual function.

Public Bulk RNA-seq and ScRNA-seq data analysis

Pseudobulk expression matrix. To investigate the differences between colorectal cancer (including mismatch repair-deficient (MMRd) and mismatch repair-proficient (MMRd) tumors) and adjacent normal tissues, we conducted an integrated single-cell pseudobulk analysis of 100 previously published scRNA-seq datasets (GEO: GSE178341). The pseudobulk expression matrix was constructed by merging the single-cell gene read counts from each sample via the average expression function of Seurat. Then, the DEGs from the tumor groups compared to those from the adjacent normal groups were identified using DESeq2 (v1.26.0),[69] and the genes with an absolute log2-fold change > 0.25 and Bonferroni-adjusted P values < 0.05 were subjected to downstream analysis. The immune cell markers, immune checkpoints, tumor markers and fibroblast markers in tumors and adjacent normal tissues were visualized by ComplexHeatmap (v2.0.0).[70]

Exhaustion signature score calculation

The exhausted signature was composed of eight typical genes that have been reported: *PDCD1*, *HAVCR2*, *TOX*, *LAG3*, *CTLA4*, *TIGIT*, *EOMES*, and *ENTPD1*. We calculated the Spearman's correlation between every two exhaustion characteristics in T cells, including $CD8^+$ T cells and $CD4^+$ T cells, from all samples, and the results were visualized by corrplot (v0.90) (https://github.com/taiyun/corrplot).

For the scRNA-seq data, we calculated module scores for the exhaustion signature with the Seurat function AddModuleScore per cell and compared the differences between the tumor and adjacent groups. For the bulk RNA-seq data, module scores for the exhaustion signature were computed using the gsva function from GSVA (v1.36.3),[71] employing the ssgsea method.

Survival analysis

To explore the relationship between the exhaustion signature and patient prognosis, we downloaded data on colorectal cancer patients from the TCGA[72] database in UCSC Xena[73]

(https://xenabrowser.net/datapages/?cohort=TCGA%20Colon%20and%20Rectal%20Cancer%20(COADREAD)&addHub=https%253A%252F%252Fgdc.xenahubs.net&removeHub=https%3A%2F%2Fxena.treehouse.gi.ucsc.edu%3A443). Patients were divided into high- and low-risk groups based on the 80th percentile risk score. K□M curves were used to compare the prognostic differences between the two groups through the survfit function of the R package survival (v3.2-13) (https://cran.r-project.org/web/packages/survival/index.html).

GO enrichment

The enrichGO and enrichKEGG of the R package ClusterProfiler (v4.9.0.002) were used to perform Gene Ontology (GO) and Kyoto Encyclopedia of Genes and Genomes (KEGG) analyses via the org.Mm.eg.db (v3.18.0) package. The results were visualized using the dotplot function of the R package enrichplot (v1.20.0) (https://github.com/YuLab-SMU/enrichplot).

Gene Set Enrichment Analysis

Gene Set Enrichment Analysis (GSEA) was performed using the ClusterProfiler (v4.9.0.002) package. Genes were initially sorted based on their log2-fold change. The enrichment was then performed using the gseGO function with the org.Mm.eg.db (v3.18.0) package. Visualization was achieved with the GseaVis (v0.0.5, github.com/junjunlab/GseaVis) package.

Statistics and reproducibility

All the statistical analyses were performed using Prism 10 (GraphPad). The data are presented as the mean ± SEM, and two-tailed Student's t test, one-way ANOVA, or two-way ANOVA was used as indicated in the figure legends. The exact value of n (number of biological or experimental replicates) can be found in the figure legends, and the exact P values are indicated in the graphed data. A P value < 0.05 was considered to indicate statistical significance. Most experiments were carried out at least two or three times, and the findings of all key experiments were reliably reproduced.

Data and Code Availability

All the raw mouse sequencing data have been deposited in the CNCB (https://ngdc.cncb.ac.cn/) BIG subproject under accession number PRJCA027119. All sequencing data are publicly available as of the date of publication.

The software and R package used in this paper are public or previously reported tools. The methods refer to the official suggestions of the tools, and the pipeline running the tools was described in the methods section of the manuscript, which did not involve the newly developed codes or tools. The codes supporting the current study are available from the corresponding authors upon request.

Conflicts of interest

The authors declare no potential conflicts of interest.

Authors' Contributions

HJ, YHL and PW designed the research; HK, PW and HJ wrote the paper; ZGZ, DC and BH supervised the clinical research design; Lu C and HBS supervised the scRNA-seq data analysis; NWK, LBH and HK collected the clinical samples; HK, JY, QXY and Lang C analyzed the clinical sample data; QXY, HK and PPM scRNA-seq data; XJW, SQD and CC performed the CRISPR knockdown of FAK; XJW, CWW, DX and HK generated the *in vivo* mouse models; PM and YP supervised the *in vivo* studies; HK, XY and YD performed the mIHC and analyzed the data; and DFZ and Lu C proofread the paper.

Acknowledgments

The authors thank the Laboratory of Digestive Surgery, West China Hospital, for clinical sample preparation and quality control (QC) validation. The authors thank Xiaogang Wang for providing the HALO image analysis platform. The authors thank Haichuan Ma for providing the structure prediction analysis of FAK-*Sp1* promoter binding. This work was supported by the following funding: Natural Science Foundation of China grants #82073158 (HJ), #82072615 (YHL) and #82273274 and the Leading Goose R&D Program of Zhejiang (2024c03142 to YHL).

References

1. Dekker, E., Tanis, P.J., Vleugels, J.L.A., Kasi, P.M., and Wallace, M.B. (2019). Colorectal cancer. Lancet *394*, 1467–1480. https://doi.org/10.1016/S0140-6736(19)32319-0.

2. Kuipers, E.J., Grady, W.M., Lieberman, D., Seufferlein, T., Sung, J.J., Boelens, P.G., van de Velde, C.J.H., and Watanabe, T. (2015). Colorectal cancer. Nat Rev Dis Primers *1*, 15065. https://doi.org/10.1038/nrdp.2015.65.

3. Ciombor, K.K., Wu, C., and Goldberg, R.M. (2015). Recent therapeutic advances in the treatment of colorectal cancer. Annu Rev Med *66*, 83–95. https://doi.org/10.1146/annurev-med-051513-102539.

4. Cañellas-Socias, A., Sancho, E., and Batlle, E. (2024). Mechanisms of metastatic colorectal cancer. Nat Rev Gastroenterol Hepatol. https://doi.org/10.1038/s41575-024-00934-z.

5. Biller, L.H., and Schrag, D. (2021). Diagnosis and Treatment of Metastatic Colorectal Cancer: A Review. JAMA *325*, 669–685. https://doi.org/10.1001/jama.2021.0106.

6. O'Donnell, J.S., Teng, M.W.L., and Smyth, M.J. (2019). Cancer immunoediting and resistance to T cell-based immunotherapy. Nat Rev Clin Oncol *16*, 151–167. https://doi.org/10.1038/s41571-018-0142-8.

7. Finck, A.V., Blanchard, T., Roselle, C.P., Golinelli, G., and June, C.H. (2022). Engineered cellular immunotherapies in cancer and beyond. Nat Med *28*, 678–689. https://doi.org/10.1038/s41591-022-01765-8.

8. Tjader, N.P., and Toland, A.E. (2024). Immunotherapy for colorectal cancer: insight from inherited genetics. Trends Cancer *10*, 444–456. https://doi.org/10.1016/j.trecan.2024.01.008.

9. Weng, J., Li, S., Zhu, Z., Liu, Q., Zhang, R., Yang, Y., and Li, X. (2022). Exploring immunotherapy in colorectal cancer. J Hematol Oncol *15*, 95. https://doi.org/10.1186/s13045-022-01294-4.

10. Fan, A., Wang, B., Wang, X., Nie, Y., Fan, D., Zhao, X., and Lu, Y. (2021). Immunotherapy in colorectal cancer: current achievements and future perspective. Int J Biol Sci *17*, 3837–3849. https://doi.org/10.7150/ijbs.64077.

11. Vilar, E., and Gruber, S.B. (2010). Microsatellite instability in colorectal cancer-the stable evidence. Nat Rev Clin Oncol *7*, 153–162. https://doi.org/10.1038/nrclinonc.2009.237.

12. Wang, C., and Fakih, M. (2021). Targeting MSS colorectal cancer with immunotherapy: are we turning the corner? Expert Opin Biol Ther *21*, 1347–1357. https://doi.org/10.1080/14712598.2021.1933940.

13. Chen, D.S., and Mellman, I. (2013). Oncology meets immunology: the cancer-immunity cycle. Immunity *39*, 1–10. https://doi.org/10.1016/j.immuni.2013.07.012.

14. Mellman, I., Chen, D.S., Powles, T., and Turley, S.J. (2023). The cancer-immunity cycle: Indication, genotype, and immunotype. Immunity *56*, 2188–2205. https://doi.org/10.1016/j.immuni.2023.09.011.

15. Kamali Zonouzi, S., Pezeshki, P.S., Razi, S., and Rezaei, N. (2022). Cancer-associated fibroblasts in colorectal cancer. Clin Transl Oncol *24*, 757–769. https://doi.org/10.1007/s12094-021-02734-2.

16. Baessler, A., and Vignali, D.A.A. (2024). T Cell Exhaustion. Annu Rev Immunol. https://doi.org/10.1146/annurev-immunol-090222-110914.

17. Yang, L., Li, A., Lei, Q., and Zhang, Y. (2019). Tumor-intrinsic signaling pathways: key roles in the regulation of the immunosuppressive tumor microenvironment. J Hematol Oncol *12*, 125. https://doi.org/10.1186/s13045-019-0804-8.

18. Binnewies, M., Roberts, E.W., Kersten, K., Chan, V., Fearon, D.F., Merad, M., Coussens, L.M., Gabrilovich, D.I., Ostrand-Rosenberg, S., Hedrick, C.C., et al. (2018). Understanding the tumor immune microenvironment (TIME) for effective therapy. Nat Med *24*, 541–550. https://doi.org/10.1038/s41591-018-0014-x.

19. Ganesh, K., Stadler, Z.K., Cercek, A., Mendelsohn, R.B., Shia, J., Segal, N.H., and Diaz, L.A. (2019). Immunotherapy in colorectal cancer: rationale, challenges and potential. Nat Rev Gastroenterol Hepatol *16*, 361–375. https://doi.org/10.1038/s41575-019-0126-x.

20. Jiang, W., He, Y., He, W., Wu, G., Zhou, X., Sheng, Q., Zhong, W., Lu, Y., Ding, Y., Lu, Q., et al. (2021). Exhausted CD8+T Cells in the Tumor Immune Microenvironment: New Pathways to Therapy. Front. Immunol. *11*. https://doi.org/10.3389/fimmu.2020.622509.

21. Merritt, C.R., Ong, G.T., Church, S.E., Barker, K., Danaher, P., Geiss, G., Hoang, M., Jung, J., Liang, Y., McKay-Fleisch, J., et al. (2020). Multiplex digital spatial profiling of proteins and RNA in fixed tissue. Nat Biotechnol *38*, 586–599. https://doi.org/10.1038/s41587-020-0472-9.

22. Pelka, K., Hofree, M., Chen, J.H., Sarkizova, S., Pirl, J.D., Jorgji, V., Bejnood, A., Dionne, D., Ge, W.H., Xu, K.H., et al. (2021). Spatially organized multicellular immune hubs in human colorectal cancer. Cell *184*, 4734-4752.e20. https://doi.org/10.1016/j.cell.2021.08.003.

23. Le, D.T., Durham, J.N., Smith, K.N., Wang, H., Bartlett, B.R., Aulakh, L.K., Lu, S., Kemberling, H., Wilt, C., Luber, B.S., et al. (2017). Mismatch repair deficiency predicts response of solid tumors to PD-1 blockade. Science *357*, 409–413. https://doi.org/10.1126/science.aan6733.

24. Newman, A.M., Steen, C.B., Liu, C.L., Gentles, A.J., Chaudhuri, A.A., Scherer, F., Khodadoust, M.S., Esfahani, M.S., Luca, B.A., Steiner, D., et al. (2019). Determining cell type abundance and expression from bulk tissues with digital cytometry. Nat Biotechnol *37*, 773–782. https://doi.org/10.1038/s41587-019-0114-2.

25. Thul, P.J., and Lindskog, C. (2018). The human protein atlas: A spatial map of the human proteome. Protein Sci *27*, 233–244. https://doi.org/10.1002/pro.3307.

26. Li, T., Fu, J., Zeng, Z., Cohen, D., Li, J., Chen, Q., Li, B., and Liu, X.S. (2020). TIMER2.0 for analysis of tumor-infiltrating immune cells. Nucleic Acids Res *48*, W509–W514. https://doi.org/10.1093/nar/gkaa407.

27. Zhang, J., Li, W., Wang, W., Chen, Q., Xu, Z., Deng, M., Zhou, L., and He, G. (2023). Dual roles of FAK in tumor angiogenesis: A review focused on pericyte FAK. Eur J Pharmacol *947*, 175694. https://doi.org/10.1016/j.ejphar.2023.175694.

28. Tanaka, T., Narazaki, M., and Kishimoto, T. (2014). IL-6 in Inflammation, Immunity, and Disease. Cold Spring Harbor Perspectives in Biology *6*, a016295–a016295. https://doi.org/10.1101/cshperspect.a016295.

29. Johnson, D.E., O'Keefe, R.A., and Grandis, J.R. (2018). Targeting the IL-6/JAK/STAT3 signalling axis in cancer. Nat Rev Clin Oncol *15*, 234–248. https://doi.org/10.1038/nrclinonc.2018.8.

30. Hegde, P.S., and Chen, D.S. (2020). Top 10 Challenges in Cancer Immunotherapy. Immunity *52*, 17–35. https://doi.org/10.1016/j.immuni.2019.12.011.

31. Galon, J., Costes, A., Sanchez-Cabo, F., Kirilovsky, A., Mlecnik, B., Lagorce-Pagès, C., Tosolini, M., Camus, M., Berger, A., Wind, P., et al. (2006). Type, density, and location of immune cells within human colorectal tumors predict clinical outcome. Science *313*, 1960–1964. https://doi.org/10.1126/science.1129139.

32. Brosseau, J.-P., and Le, L.Q. (2019). Heterozygous Tumor Suppressor Microenvironment in Cancer Development. Trends Cancer *5*, 541–546. https://doi.org/10.1016/j.trecan.2019.07.004.

33. Jiang, H., Hegde, S., Knolhoff, B.L., Zhu, Y., Herndon, J.M., Meyer, M.A., Nywening, T.M., Hawkins, W.G., Shapiro, I.M., Weaver, D.T., et al. (2016). Targeting Focal Adhesion Kinase Renders Pancreatic Cancers Responsive to Checkpoint Immunotherapy. Nat Med *22*, 851–860. https://doi.org/10.1038/nm.4123.

34. Jiang, H., Liu, X., Knolhoff, B.L., Hegde, S., Lee, K.B., Jiang, H., Fields, R.C., Pachter, J.A., Lim, K.-H., and DeNardo, D.G. (2020). The development of resistance to FAK inhibition in pancreatic cancer is linked to stromal depletion. Gut *69*, 122–132. https://doi.org/10.1136/gutjnl-2018-317424.

35. Patsoukis, N., Wang, Q., Strauss, L., and Boussiotis, V.A. (2020). Revisiting the PD-1 pathway. Sci Adv *6*, eabd2712. https://doi.org/10.1126/sciadv.abd2712.

36. Rowshanravan, B., Halliday, N., and Sansom, D.M. (2018). CTLA-4: a moving target in immunotherapy. Blood *131*, 58–67. https://doi.org/10.1182/blood-2017-06-741033.

37. Wright, J.J., Powers, A.C., and Johnson, D.B. (2021). Endocrine toxicities of immune checkpoint inhibitors. Nat Rev Endocrinol *17*, 389–399. https://doi.org/10.1038/s41574-021-00484-3.

38. Rotte, A., Jin, J.Y., and Lemaire, V. (2018). Mechanistic overview of immune checkpoints to support the rational design of their combinations in cancer immunotherapy. Ann Oncol *29*, 71–83. https://doi.org/10.1093/annonc/mdx686.

39. Topalian, S.L., Hodi, F.S., Brahmer, J.R., Gettinger, S.N., Smith, D.C., McDermott, D.F., Powderly, J.D., Carvajal, R.D., Sosman, J.A., Atkins, M.B., et al. (2012). Safety, activity, and immune correlates of anti-PD-1 antibody in cancer. N Engl J Med *366*, 2443–2454. https://doi.org/10.1056/NEJMoa1200690.

40. Chen, L., and Han, X. (2015). Anti-PD-1/PD-L1 therapy of human cancer: past, present, and future. J Clin Invest *125*, 3384–3391. https://doi.org/10.1172/JCI80011.

41. Wolf, Y., Anderson, A.C., and Kuchroo, V.K. (2020). TIM3 comes of age as an inhibitory receptor. Nat Rev Immunol *20*, 173–185. https://doi.org/10.1038/s41577-019-0224-6.

42. Acharya, N., Sabatos-Peyton, C., and Anderson, A.C. (2020). Tim-3 finds its place in the cancer immunotherapy landscape. J Immunother Cancer *8*, e000911. https://doi.org/10.1136/jitc-2020-000911.

43. Saleh, R., Taha, R.Z., Toor, S.M., Sasidharan Nair, V., Murshed, K., Khawar, M., Al-Dhaheri, M., Petkar, M.A., Abu Nada, M., and Elkord, E. (2020). Expression of immune checkpoints and T cell exhaustion markers in early and advanced stages of colorectal cancer. Cancer Immunol Immunother *69*, 1989–1999. https://doi.org/10.1007/s00262-020-02593-w.

44. Huang, Y.-H., Zhu, C., Kondo, Y., Anderson, A.C., Gandhi, A., Russell, A., Dougan, S.K., Petersen, B.-S., Melum, E., Pertel, T., et al. (2015). CEACAM1 regulates TIM-3-mediated tolerance and exhaustion. Nature *517*, 386–390. https://doi.org/10.1038/nature13848.

45. Sauer, N., Janicka, N., Szlasa, W., Skinderowicz, B., Kołodzińska, K., Dwernicka, W., Oślizło, M., Kulbacka, J., Novickij, V., and Karłowicz-Bodalska, K. (2023). TIM-3 as a

promising target for cancer immunotherapy in a wide range of tumors. Cancer Immunol Immunother *72*, 3405–3425. https://doi.org/10.1007/s00262-023-03516-1.

46. Duong, B., Banskota, P., and Falchook, G.S. (2024). T cell Immunoglobulin and Mucin Domain Containing Protein 3 (TIM-3) Inhibitors in Oncology Clinical Trials: A Review. J Immunother Precis Oncol *7*, 89–96. https://doi.org/10.36401/JIPO-23-4.

47. Philip, M., and Schietinger, A. (2022). CD8+ T cell differentiation and dysfunction in cancer. Nat Rev Immunol *22*, 209–223. https://doi.org/10.1038/s41577-021-00574-3.

48. I, S., K, S., V, C., Sa, F.M., S, C.-C., D, P.F., Sj, C., L, S., D, G., S, P., et al. (2019). Intratumoral Tcf1+PD-1+CD8+ T Cells with Stem-like Properties Promote Tumor Control in Response to Vaccination and Checkpoint Blockade Immunotherapy. Immunity *50*. https://doi.org/10.1016/j.immuni.2018.12.021.

49. Escobar, G., Tooley, K., Oliveras, J.P., Huang, L., Cheng, H., Bookstaver, M.L., Edwards, C., Froimchuk, E., Xue, C., Mangani, D., et al. (2023). Tumor immunogenicity dictates reliance on TCF1 in CD8+ T cells for response to immunotherapy. Cancer Cell, S1535-6108(23)00273-8. https://doi.org/10.1016/j.ccell.2023.08.001.

50. Lim, S.-T., Chen, X.L., Lim, Y., Hanson, D.A., Vo, T.-T., Howerton, K., Larocque, N., Fisher, S.J., Schlaepfer, D.D., and Ilic, D. (2008). Nuclear FAK promotes cell proliferation and survival through FERM-enhanced p53 degradation. Mol Cell *29*, 9–22. https://doi.org/10.1016/j.molcel.2007.11.031.

51. Serrels, A., Lund, T., Serrels, B., Byron, A., McPherson, R.C., von Kriegsheim, A., Gómez-Cuadrado, L., Canel, M., Muir, M., Ring, J.E., et al. (2015). Nuclear FAK controls chemokine transcription, Tregs, and evasion of anti-tumor immunity. Cell *163*, 160–173. https://doi.org/10.1016/j.cell.2015.09.001.

52. Abramson, J., Adler, J., Dunger, J., Evans, R., Green, T., Pritzel, A., Ronneberger, O., Willmore, L., Ballard, A.J., Bambrick, J., et al. (2024). Accurate structure prediction of biomolecular interactions with AlphaFold 3. Nature *630*, 493–500. https://doi.org/10.1038/s41586-024-07487-w.

53. Dawson, J.C., Serrels, A., Stupack, D.G., Schlaepfer, D.D., and Frame, M.C. (2021). Targeting FAK in anticancer combination therapies. Nat Rev Cancer *21*, 313–324. https://doi.org/10.1038/s41568-021-00340-6.

54. Ozmadenci, D., Shankara Narayanan, J.S., Andrew, J., Ojalill, M., Barrie, A.M., Jiang, S., Iyer, S., Chen, X.L., Rose, M., Estrada, V., et al. (2022). Tumor FAK orchestrates immunosuppression in ovarian cancer via the CD155/TIGIT axis. Proc Natl Acad Sci U S A *119*, e2117065119. https://doi.org/10.1073/pnas.2117065119.

55. Bankhead, P., Loughrey, M.B., Fernández, J.A., Dombrowski, Y., McArt, D.G., Dunne, P.D., McQuaid, S., Gray, R.T., Murray, L.J., Coleman, H.G., et al. (2017). QuPath: Open source software for digital pathology image analysis. Sci Rep *7*, 16878. https://doi.org/10.1038/s41598-017-17204-5.

56. Bolger, A.M., Lohse, M., and Usadel, B. (2014). Trimmomatic: a flexible trimmer for Illumina sequence data. Bioinformatics *30*, 2114–2120. https://doi.org/10.1093/bioinformatics/btu170.

57. Langmead, B., and Salzberg, S.L. (2012). Fast gapped-read alignment with Bowtie 2. Nat Methods *9*, 357–359. https://doi.org/10.1038/nmeth.1923.

58. Li, H., Handsaker, B., Wysoker, A., Fennell, T., Ruan, J., Homer, N., Marth, G., Abecasis, G., Durbin, R., and 1000 Genome Project Data Processing Subgroup (2009). The Sequence Alignment/Map format and SAMtools. Bioinformatics *25*, 2078–2079. https://doi.org/10.1093/bioinformatics/btp352.

59. Zhang, Y., Liu, T., Meyer, C.A., Eeckhoute, J., Johnson, D.S., Bernstein, B.E., Nusbaum, C., Myers, R.M., Brown, M., Li, W., et al. (2008). Model-based analysis of ChIP-Seq (MACS). Genome Biol *9*, R137. https://doi.org/10.1186/gb-2008-9-9-r137.

60. Yu, G., Wang, L.-G., and He, Q.-Y. (2015). ChIPseeker: an R/Bioconductor package for ChIP peak annotation, comparison and visualization. Bioinformatics *31*, 2382–2383. https://doi.org/10.1093/bioinformatics/btv145.

61. Wu, T., Hu, E., Xu, S., Chen, M., Guo, P., Dai, Z., Feng, T., Zhou, L., Tang, W., Zhan, L., et al. (2021). clusterProfiler 4.0: A universal enrichment tool for interpreting omics data. Innovation (Camb) *2*, 100141. https://doi.org/10.1016/j.xinn.2021.100141.

62. Ramírez, F., Ryan, D.P., Grüning, B., Bhardwaj, V., Kilpert, F., Richter, A.S., Heyne, S., Dündar, F., and Manke, T. (2016). deepTools2: a next generation web server for deep-sequencing data analysis. Nucleic Acids Res *44*, W160-165. https://doi.org/10.1093/nar/gkw257.

63. Ramírez, F., Bhardwaj, V., Arrigoni, L., Lam, K.C., Grüning, B.A., Villaveces, J., Habermann, B., Akhtar, A., and Manke, T. (2018). High-resolution TADs reveal DNA sequences underlying genome organization in flies. Nat Commun *9*, 189. https://doi.org/10.1038/s41467-017-02525-w.

64. Zheng, G.X.Y., Terry, J.M., Belgrader, P., Ryvkin, P., Bent, Z.W., Wilson, R., Ziraldo, S.B., Wheeler, T.D., McDermott, G.P., Zhu, J., et al. (2017). Massively parallel digital transcriptional profiling of single cells. Nat Commun *8*, 14049. https://doi.org/10.1038/ncomms14049.

65. Butler, A., Hoffman, P., Smibert, P., Papalexi, E., and Satija, R. (2018). Integrating single-cell transcriptomic data across different conditions, technologies, and species. Nat Biotechnol *36*, 411–420. https://doi.org/10.1038/nbt.4096.

66. De Falco, A., Caruso, F., Su, X.-D., Iavarone, A., and Ceccarelli, M. (2023). A variational algorithm to detect the clonal copy number substructure of tumors from scRNA-seq data. Nat Commun *14*, 1074. https://doi.org/10.1038/s41467-023-36790-9.

67. Street, K., Risso, D., Fletcher, R.B., Das, D., Ngai, J., Yosef, N., Purdom, E., and Dudoit, S. (2018). Slingshot: cell lineage and pseudotime inference for single-cell transcriptomics. BMC Genomics *19*, 477. https://doi.org/10.1186/s12864-018-4772-0.

68. Jin, S., Plikus, M.V., and Nie, Q. (2023). CellChat for systematic analysis of cell-cell communication from single-cell and spatially resolved transcriptomics. Preprint at bioRxiv, https://doi.org/10.1101/2023.11.05.565674 https://doi.org/10.1101/2023.11.05.565674.

69. Love, M.I., Huber, W., and Anders, S. (2014). Moderated estimation of fold change and dispersion for RNA-seq data with DESeq2. Genome Biol *15*, 550. https://doi.org/10.1186/s13059-014-0550-8.

70. Gu, Z., Eils, R., and Schlesner, M. (2016). Complex heatmaps reveal patterns and correlations in multidimensional genomic data. Bioinformatics *32*, 2847–2849. https://doi.org/10.1093/bioinformatics/btw313.

71. Hänzelmann, S., Castelo, R., and Guinney, J. (2013). GSVA: gene set variation analysis for microarray and RNA-seq data. BMC Bioinformatics *14*, 7. https://doi.org/10.1186/1471-2105-14-7.

72. Liu, J., Lichtenberg, T., Hoadley, K.A., Poisson, L.M., Lazar, A.J., Cherniack, A.D., Kovatich, A.J., Benz, C.C., Levine, D.A., Lee, A.V., et al. (2018). An Integrated TCGA Pan-Cancer Clinical Data Resource to Drive High-Quality Survival Outcome Analytics. Cell *173*, 400-416.e11. https://doi.org/10.1016/j.cell.2018.02.052.

73. Goldman, M.J., Craft, B., Hastie, M., Repečka, K., McDade, F., Kamath, A., Banerjee, A., Luo, Y., Rogers, D., Brooks, A.N., et al. (2020). Visualizing and interpreting cancer genomics data via the Xena platform. Nat Biotechnol *38*, 675–678. https://doi.org/10.1038/s41587-020-0546-8.

Figure legends

Fig. 1 Characterization of the tumor immune microenvironment through scRNA sequencing and spatial proteomic profiling.

a, t-SNEs (t-distributed stochastic neighbor embedding) by major cell partitions of all samples (left). MMRp tumors (n = 35), MMRd tumors (n = 29), and MMRp and MMRd normal (n=36) from 62 individuals (34 MMRd and 28 MMRp). **b,** Heatmap of immune cell marker, immune checkpoint, tumor marker and fibroblast marker expression in tumor cells and adjacent normal cells from MMRp and MMRd CRC patients. **c,** Unsupervised hierarchically clustered heatmap of protein expression in regions of interest in tumor or adjacent normal tissues from CRC patients (n=9) based on DSP data. **d,** Correlations between two checkpoints. **e,** Exhaustion score

comparison between normal and tumor tissues. The data are presented as the means ± s.e.m.ss (normal, n =36; tumor, n = 64), as determined by two-tailed unpaired t tests. **f,** OS in patients with high and low exhaustion scores according to Kaplan□Meier analysis of TCGA CRC datasets.

Fig. 2 Spatial TIL exhaustion is associated with hyperactivation of FAK signaling.

a, Principal component analysis (PCA) plot of single-cell RNA-seq data for MMRp tumors, MMRd tumors, MMRp normal tissues and MMRd normal tissues. **b,** Volcano plot of differentially expressed genes (DEGs) between normal and tumor tissues, log2 (fold change) ≥ 0.1. **c,** Enrichment analysis of DEGs between normal and tumor tissues using KEGG/GO pathways. **d,** t-SNE plot of all cells shown in **Fig. 1a,** with *PTK2*-expressing cells colored according to cell density. **e,** t-SNE plot of tumor cells in scRNA-seq data clustered into 11 subtypes. **f,** t-SNE plot of tumor cells shown in **Fig. 2e**, with *PTK2*-expressing cells colored according to cell density. **g,** *PTK2* expression in 11 subtypes of tumor cells. **h,** *PTK2* expression in the MMRp, MMRd, MMRP and MMRd normal groups. **i,** Representative immunohistochemistry images and analysis of total and phosphorylated FAK (p-FAK, Tyr397) in human adjacent normal colon and CRC tumor tissues. The data are presented as the means ± s.e.m.ss (n = 5), as determined by two-tailed unpaired t tests. **j,** Simple linear regression correlation plot of PD-1/TIM-3/LAG-3 expression per unit CD45 expression from the DSP data with the percentage of pFAK area. The data are presented as the means ± 95% confidence intervals (95% CIs). **k,** Representative merged images of multiplexed staining for DAPI (blue), CK19 (green), pFAK (red), CD3 (cyan) and TIM-3 (yellow). **l,** Representative composite images of rectal carcinoma tissue from the pFAK high or low groups with multiplexed staining and imaging of five individual markers (DAPI, blue; CK19, green; pFAK, red; CD3, cyan; TIM-3, yellow) (left) and a representative proximity distance map showing TIM-3^+ TILs within or outside a radius of 100 μm from the nuclear center of tumor cells ($pFAK^+CK19^+$ cells) (right). **m,** Comparisons of the percentage of $pFAK^+$ cells among all cells between the pFAK high group (ROIs, n=28) and the pFAK lwo group (ROIs, n=17). The data are presented as the means ± s.e.m.s, as determined by two-tailed unpaired t tests. **n,** Comparisons of the percentages of TIM-3^+ TILs among all cells between the pFAK high group (ROIs, n=28) and the pFAK lwo group (ROIs, n=17). The data are presented as the means ± s.e.m.s, as determined by two-tailed

unpaired t tests. **o,** Comparisons of the percentage of TIM-3$^+$ TILs within 100 μm from pFAK$^+$CK19$^+$ cells between the pFAK high group (ROIs, n=28) and pFAK low group (ROIs, n=17). The data are presented as the means ± s.e.m.s, as determined by two-tailed unpaired t tests. **p,** Schematic depicting the spatial distribution of TIM-3$^+$ cells in CRC patients with high or low pFAK expression.

Fig. 3 FAK inhibition leads to stable disease progression by reshaping the TIME.

a, Growth rate of MC38 subcutaneous tumors treated with a FAK inhibitor (FAKi, VS-4718, 50 mg/kg) or vehicle. Vehicle or FAKi was administered intragastrically twice per day. The data are presented as the mean ± s.e.m. (vehicle, n = 5; FAKi, n = 6), as determined by one-way ANOVA. **b,** Growth rate of subcutaneous CT26 tumors treated with a FAK inhibitor (FAKi, VS-4718, 50 mg/kg) or vehicle. Vehicle or FAKi was administered intragastrically twice per day. The data are presented as the means ± s.e.m.s (n = 6 mice per group), as determined by one-way ANOVA. **c,** UMAP plot of 47,442 cells from vehicle (n = 2)- or FAKi (n = 3)-treated tumor tissues, colored according to annotated cell type. **d,** Relative fraction of each cluster in **Fig. 3c of** vehicle- or FAKi-treated tumors**. e,** Numbers of differentially expressed genes (up- or downregulated) in each cluster. **f,** Differentially expressed genes in CD8$^+$ T cells from the FAKi group versus those from the vehicle group. **g-h,** Gene set enrichment analysis (GSEA) of the scRNA-seq data of all cells revealed enrichment of genes related to the positive regulation of T-cell differentiation and activation. **i,** Percentages of *Pdcd-1*^{high} and *Pdcd-1*^{low} CD8$^+$ T cells among CD8$^+$ T cells from vehicle- or FAKi-treated tumors. **j,** Trajectory analysis of CD8$^+$ T cells in vehicle- or FAKi-treated tumors. Three branches of stem-like CD8$^+$ T cells, proliferating CD8$^+$ T cells and exhausted CD8$^+$ T cells were clustered. **k,** Expression of *Slamf6*, *Tcf7*, *Birc5*, *Top2a*, *Pdcd1* and *Tox* in stem-like CD8$^+$ T cells, proliferating CD8$^+$ T cells and exhausted CD8$^+$ T cells. **l,** Percentages of stem-like CD8$^+$ T cells, proliferating CD8$^+$ T cells and exhausted CD8$^+$ T cells among CD8$^+$ T cells in vehicle- or FAKi-treated tumors. **m-n,** Inferred PD-L1 and TNF signaling networks in FAKi- or vehicle-treated tumors. **o,** Representative mIHC images of DAPI (blue), CD8 (pink), TIM-3 (yellow), TOX (red), PD-1 (cyan), and TCF-1 (green) in tumors from vehicle- or FAKi-treated mice. **p,** Representative image and percentage of PD-1$^+$TIM-3$^+$TOX$^+$ CD8$^+$ T cells among CD8$^+$ T cells in CT26 tumors from vehicle (n=4)- or FAKi (n=5)-treated mice. The data are presented as the means ± s.e.m.s, as determined by two-tailed unpaired t tests.

q, Representative image and percentage of TCF-1$^+$ CD8$^+$ cells among CD8$^+$ cells in CT26 tumors from vehicle-treated mice (n=4) or FAKi-treated mice (n=5). The data are presented as the means ± s.e.m.s, as determined by two-tailed unpaired t tests. **r,** Percentages of exhausted (TIM-3$^+$PD-1$^+$) CD8$^+$ T cells among CD8$^+$ T cells determined by flow cytometry in CT26 tumors from vehicle-treated mice (n=5) and FAKi-treated mice (n=4). The data are presented as the means ± s.e.m.s, as determined by two-tailed unpaired t tests. **s,** Percentages of cytotoxic (GZMB$^+$) CD8$^+$ T cells among CD8$^+$ T cells in MC38 tumors from vehicle-treated mice (n=6) and FAKi-treated mice (n=6) determined by flow cytometry. The data are presented as the means ± s.e.m.s, as determined by two-tailed unpaired t tests.

Fig. 4 Knockdown of tumor-intrinsic FAK reversed CD8$^+$ T-cell exhaustion in colorectal tumors.

a, Western blot of total FAK expression in Cas9 or sgPtk2 CT26 cell lysates. **b,** Cell viability measurements of Cas9 or sgPtk2 CT26 cells on day 3 and day 5. **c,** Tumor growth curves of Cas9- and FAK-knockdown CT26 tumors in BALB/c-nude mice. The data are presented as the means ± s.e.m.ss (n = 5 mice per group), as determined by one-way ANOVA. **d,** Growth curves of Cas9- and FAK-knockdown CT26 tumors in BALB/c mice. The data are presented as the means ± s.e.m.s (n = 7 mice per group), as determined by one-way ANOVA. **e,** UMAP plot of 87,383 cells from CT26 Cas9 (n = 2), sgPtk2_1 (n = 3) and sgPtk2_2 (n = 3) tumor tissues, colored by annotated cell type. **f,** Violin map showing the expression levels of specific markers in each cell type. **g,** Relative fraction of each cluster in **Fig. 4e** in CT26 Cas9, sgPtk2_1 and sgPtk2_2 tumors. **h,** Trajectory analysis of CD8$^+$ T cells in CT26 Cas9, sgPtk2_1 and sgPtk2_2 tumors. Three branches of stem-like CD8$^+$ T cells, proliferating CD8$^+$ T cells and exhausted CD8$^+$ T cells were clustered. **i,** Inferred PD-L1 signaling networks in CT26 Cas9, sgPtk2_1 and sgPtk2_2 tumors. **j,** Representative mIHC images of Cas9, sgPtk2_1 and sgPtk2_2 tumors showing DAPI (blue), tumor cell (green), CD8 (pink), PD-1 (cyan) and TOX (red) staining. **k,** Comparisons of the percentages of exhausted T cells (PD-1$^+$TIM-3$^+$), terminally exhausted T cells (PD-1$^+$TIM-3$^+$TOX$^+$) and stem-like T cells (TCF-1$^+$) among CD8$^+$ T cells within intratumoral regions from Cas9 tumors, sgPtk2_1 tumors and sgPtk2_2 tumors. The data are presented as the means ± s.e.m.s (n = 6 ROIs per group), as determined by one-way ANOVA. **l,** Schematic depicting the *in vitro* coculture system of CD8$^+$ T cells and CT26 Cas9 or sgPtk2

tumor cells. **m,** Percentage of TIM-3$^+$TOX$^+$CD8$^+$ T cells among CD8$^+$ T cells determined by flow cytometry from a coculture system of CD8$^+$ T cells and CT26 Cas9 or sgPtk2 tumor cells. The data are presented as the means ± s.e.m.s (n = 3 per group), as determined by two-tailed unpaired t tests. **n,** Percentages of PD-1$^+$TIM-3$^+$TOX$^+$CD8$^+$ T cells among CD8$^+$ T cells determined by flow cytometry in a coculture system of CD8$^+$ T cells and CT26 Cas9 or sgPtk2 tumor cells. The data are presented as the means ± s.e.m.s (n = 3 per group), as determined by two-tailed unpaired t tests. **o,** Percentages of TCF-1$^+$CD8$^+$ T cells among CD8$^+$ T cells determined by flow cytometry in a coculture system of CD8$^+$ T cells and CT26 Cas9 or sgPtk2 tumor cells. The data are presented as the means ± s.e.m.ss (n = 3 per group), as determined by two-tailed unpaired t tests. **p,** Percentage of Ki67$^+$CD8$^+$ T cells among CD8$^+$ T cells determined by flow cytometry from a coculture system of CD8$^+$ T cells and CT26 Cas9 or sgPtk2 tumor cells. The data are presented as the means ± s.e.m.s (n = 3 per group), as determined by two-tailed unpaired t tests.

Fig. 5 Nuclear FAK promotes CD8$^+$ T cell exhaustion by transcriptionally regulating the SP1/IL-6 axis.

a, Representative mIHC images of human CRC tissue stained with DAPI (blue), PanCK (green) and FAK (red). **b,** Representative immunofluorescence staining of FAK in CT26 cells. **c,** Fluorescence colocalization analysis of FAK and DAPI in CT26 cells. **d,** Western blot showing FAK expression in the cytoplasm and nucleus of CT26 cells. **e,** CUT&Tag sequencing analysis of FAK in CT26 cells with or without FAK antibody. **f,** Distribution of peaks identified from CUT&Tag sequencing across gene regions using MACS2. **g,** Ranking of the top genes by CUT&Tag-seq using MACS2. The top transcription factors among all genes are highlighted. **h,** Representative illustration of FAK binding patterns analyzed by CUT&Tag-seq at the genomic loci of *Sp1*. The promoter regions of the three genes are highlighted in pink. **i,** Structural prediction of FAK-*Sp1* promoter binding by AlphaFold3. **j,** Real-time quantitative PCR (RT□qPCR) of the FAK binding promotor of *Sp1* in the CUT&Tag library constructed from Cas9 and sgPtk2 CT26 cells. The data are presented as the mean ± s.e.m. (n = 2 per group), as determined by one-way ANOVA. **k,** Real-time quantitative PCR (RT–qPCR) of *Sp1* transcript levels in CT26 Cas9, sgPtk2_1 and shPtk2_2 cells. The data are presented as the mean ± s.e.m. (n = 3 per group), as determined by one-way ANOVA. **l,** Representative immunofluorescence

staining of SP1 in CT26 Cas9, sgPtk2_1, and sgPtk2_2 cells. The mean fluorescence intensity was calculated and is presented as the mean ± s.e.m. (Cas9, n = 134; sgPtk2_1, n = 129; sgPtk2_2, n = 112), as determined by one-way ANOVA. **m,** Real-time quantitative PCR (RT–qPCR) of cytokine transcript levels in CT26 Cas9, sgPtk2_1, and sgPtk2_2 cells. The data are presented as the mean ± s.e.m. (n = 3 per group), as determined by two-tailed one-way ANOVA. **n,** Representative flow cytometry gating of PD-1$^+$, TIM-3$^+$ or TOX$^+$ CD8$^+$ T cells among CD8$^+$ T cells treated with or without IL-6 for 3 days or 6 days. **o,** Percentages of PD-1$^+$TOX$^+$, TIM-3$^+$TOX$^+$ and PD-1$^+$TIM-3$^+$TOX$^+$ CD8$^+$ T cells among CD8$^+$ T cells treated with or without IL-6 for 3 days or 6 days, as determined by flow cytometry. The data are presented as the means ± s.e.m.s (n = 3 per group), as determined by two-tailed unpaired t tests. **p,** Representative mIHC images of CT26 Cas9 tumors, sgPtk2_1 tumors and sgPtk2_2 tumors stained with DAPI (blue), tumor cells (green), pFAK (cyan) and IL-6 (red). **q,** Percentage of IL-6$^+$ cells among all cells from CT26 Cas9 tumors, sgPtk2_1 tumors and sgPtk2_2 tumors. The data are presented as the means ± s.e.m.s (n = 4 per group), as determined by one-way ANOVA. **r,** Percentage of pFAK$^+$ cells among all cells from CT26 Cas9 tumors, sgPtk2_1 tumors and sgPtk2_2 tumors. The data are presented as the means ± s.e.m.s (n = 4 per group), as determined by one-way ANOVA. **s,** Percentage of pFAK$^+$ tumor cells among IL-6$^+$ cells from CT26 Cas9 tumors, sgPtk2_1 tumors and sgPtk2_2 tumors. The data are presented as the means ± s.e.m.s (n = 4 per group), as determined by one-way ANOVA.

Fig. 6 Inhibition of FAK improves the efficacy of immune checkpoint blockade (ICB) therapy *in vivo*.

a, Growth curves of subcutaneous MC38 tumors treated with combination therapies. In the Immuno group, 5-Fu (20 mg/kg) combined with anti-TIM-3 (10 mg/kg) and anti-PD-1 (10 mg/kg) was used. Vehicle or FAKi was administered intragastrically twice per day. 5-Fu or vehicle was intraperitoneally administered once every two days. Isotype or anti-TIM-3 combined with anti-PD-1 was intraperitoneally administered once every 4 days. The data are presented as the means ± s.e.m.ss (n = 6 mice per group), as determined by two-way ANOVA. **b,** Growth curves of subcutaneous CT26 tumors treated with combination therapies. In the Immuno group, 5-Fu (20 mg/kg) combined with anti-TIM-3 (10 mg/kg) and anti-PD-1 (10 mg/kg) was used. Vehicle or FAKi was administered intragastrically twice per day. 5-Fu or vehicle was

intraperitoneally administered once every two days. Isotype or anti-TIM-3 combined with anti-PD-1 was intraperitoneally administered once every 4 days. The data are presented as the means ± s.e.m.s (n = 5 mice per group), as determined by two-way ANOVA. **c,** Schematics depicting the $CD45^+$ cell sorting strategy for subsequent scRNA-seq. **d,** t-SNE plot of 75,631 cells from vehicle-, immuno-, FAKi- or combination-treated tumor tissues (n = 2 per group), colored according to the annotated cell type. **e,** Relative fraction of each cluster in **Fig. 6d** in the vehicle-, immuno-, FAKi- or combination-treated groups. **f,** UMAP plot of $CD8^+$ T cells from all cells collected from the scRNA-seq data. $CD8^+$ T cells were clustered into Tprolif, Tpem, Tem and Tex subsets. Key markers of the clustering process are highlighted in the map. **g,** Relative fraction of each cluster in **Fig. 6f** in the vehicle-, immune-, FAKi- or combination-treated groups. **h,** Violin map of the expression of exhaustion markers (*Havcr2*, *Pdcd1*, and *Tox*) and cytotoxic markers (*Cd69*, *Ifngr1* and *Tnf*) in the vehicle, immuno-, FAKi- or combination-treated groups. **i,** Two trajectories (cytotoxic trajectory and exhausted trajectory) of $CD8^+$ T cells based on Slingshot and the $CD8^+$ T-cell phenotype (left) and pseudotime (right) are displayed. **j,** Plot of exhaustion and cytotoxicity markers along the cytotoxic $CD8^+$ T-cell lineage based on pseudotime. **k,** Gene set enrichment analysis of DEGs in $CD8^+$ T cells. **l,** Representative mIHC images of DAPI (blue), CD8 (pink), pSTAT3 (green), TOX (red) and TIM-3 (yellow) in tumors from vehicle-treated mice, immune-treated mice, FAKi-treated mice and combination-treated mice. **m,** Percentage of $pSTAT3^+CD8^+$ T cells among $CD8^+$ T cells in CT26 tumors from vehicle-treated mice (n = 5), immuno-treated mice (n = 5), FAKi-treated mice (n = 4) and combination-treated mice (n = 5) determined by mIHC. The data are presented as the means ± s.e.m.s, as determined by one-way ANOVA. **n,** Percentage of $TOX^+TIM\text{-}3^+CD8^+$ T cells among $CD8^+$ T cells in CT26 tumors from vehicle-treated mice (n = 5), immuno-treated mice (n = 5), FAKi-treated mice (n = 4) and combination-treated mice (n = 5) determined by mIHC. The data are presented as the means ± s.e.m.s, as determined by one-way ANOVA. **q,** Schematic of how combination therapy influences the microenvironment and the differences between high pFAK CRC and low pFAK CRC patients.

Figure1

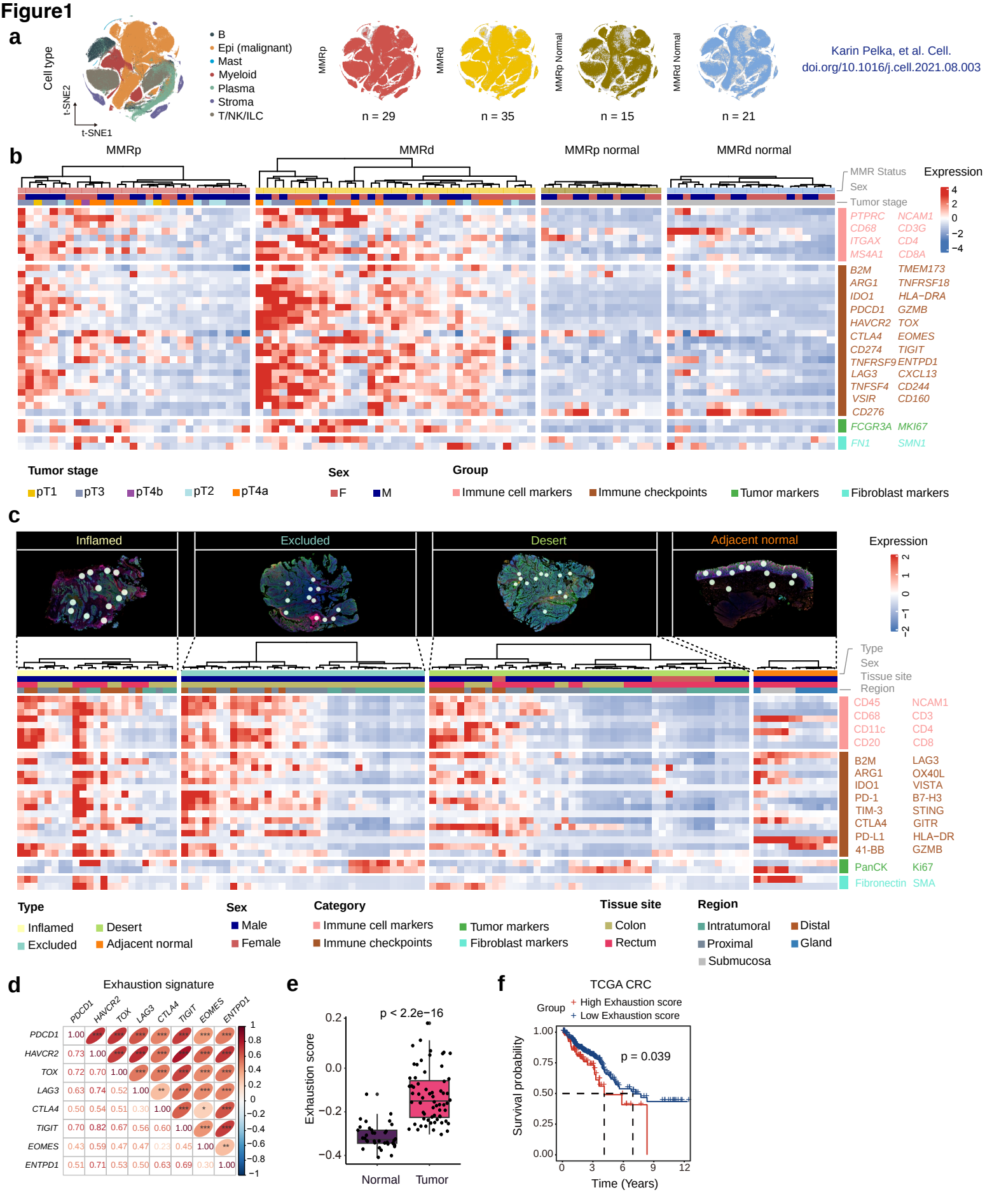

a
Cell type
t-SNE2
t-SNE1
B
Epi (malignant)
Mast
Myeloid
Plasma
Stroma
T/NK/ILC
MMRp
MMRd
MMRp Normal
MMRd Normal
n = 29
n = 35
n = 15
n = 21
Karin Pelka, et al. Cell.
doi.org/10.1016/j.cell.2021.08.003
b
MMRp
MMRd
MMRp normal
MMRd normal
MMR Status
Sex
Tumor stage
Expression
PTPRC NCAM1
CD68 CD3G
ITGAX CD4
MS4A1 CD8A
B2M TMEM173
ARG1 TNFRSF18
IDO1 HLA−DRA
PDCD1 GZMB
HAVCR2 TOX
CTLA4 EOMES
CD274 TIGIT
TNFRSF9 ENTPD1
LAG3 CXCL13
TNFSF4 CD244
VSIR CD160
CD276
FCGR3A MKI67
FN1 SMN1
Tumor stage
pT1 pT3 pT4b pT2 pT4a
Sex
F M
Group
Immune cell markers
Immune checkpoints
Tumor markers
Fibroblast markers
c
Inflamed
Excluded
Desert
Adjacent normal
Expression
Type
Sex
Tissue site
Region
CD45 NCAM1
CD68 CD3
CD11c CD4
CD20 CD8
B2M LAG3
ARG1 OX40L
IDO1 VISTA
PD-1 B7-H3
TIM-3 STING
CTLA4 GITR
PD-L1 HLA−DR
41-BB GZMB
PanCK Ki67
Fibronectin SMA
Type
Inflamed
Excluded
Desert
Adjacent normal
Sex
Male
Female
Category
Immune cell markers
Immune checkpoints
Tumor markers
Fibroblast markers
Tissue site
Colon
Rectum
Region
Intratumoral
Proximal
Submucosa
Distal
Gland
d
Exhaustion signature
PDCD1 HAVCR2 TOX LAG3 CTLA4 TIGIT EOMES ENTPD1
PDCD1 1.00 *** *** *** *** *** *** ***
HAVCR2 0.73 1.00 *** *** *** *** *** ***
TOX 0.72 0.70 1.00 *** *** *** *** ***
LAG3 0.63 0.74 0.52 1.00 ** *** *** ***
CTLA4 0.50 0.54 0.51 0.30 1.00 *** * ***
TIGIT 0.70 0.82 0.67 0.56 0.60 1.00 *** ***
EOMES 0.43 0.59 0.47 0.47 0.23 0.45 1.00 **
ENTPD1 0.51 0.71 0.53 0.50 0.63 0.69 0.30 1.00
e
p < 2.2e−16
Exhaustion score
Normal
Tumor
f
TCGA CRC
Group
High Exhaustion score
Low Exhaustion score
p = 0.039
Survival probability
Time (Years)

Figure 2

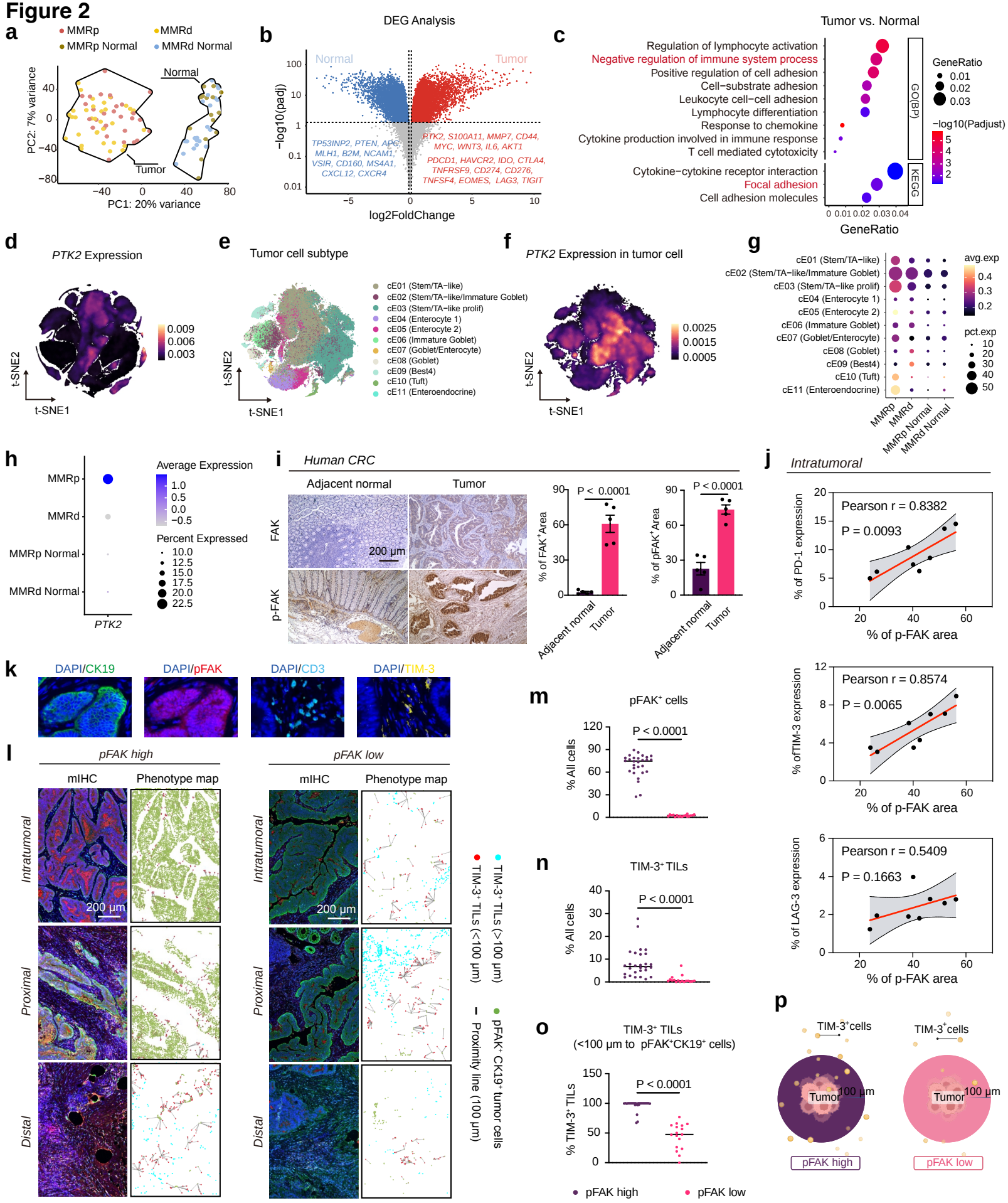
a
MMRp
MMRd
MMRp Normal
MMRd Normal
Normal
Tumor
PC2: 7% variance
PC1: 20% variance
b
DEG Analysis
Normal
Tumor
−log10(padj)
log2FoldChange
TP53INP2, PTEN, APC, MLH1, B2M, NCAM1, VSIR, CD160, MS4A1, CXCL12, CXCR4
PTK2, S100A11, MMP7, CD44, MYC, WNT3, IL6, AKT1
PDCD1, HAVCR2, IDO, CTLA4, TNFRSF9, CD274, CD276, TNFSF4, EOMES, LAG3, TIGIT
c
Tumor vs. Normal
Regulation of lymphocyte activation
Negative regulation of immune system process
Positive regulation of cell adhesion
Cell−substrate adhesion
Leukocyte cell−cell adhesion
Lymphocyte differentiation
Response to chemokine
Cytokine production involved in immune response
T cell mediated cytotoxicity
Cytokine−cytokine receptor interaction
Focal adhesion
Cell adhesion molecules
GO(BP)
KEGG
GeneRatio
−log10(Padjust)
d
PTK2 Expression
t-SNE2
t-SNE1
e
Tumor cell subtype
cE01 (Stem/TA−like)
cE02 (Stem/TA−like/Immature Goblet)
cE03 (Stem/TA−like prolif)
cE04 (Enterocyte 1)
cE05 (Enterocyte 2)
cE06 (Immature Goblet)
cE07 (Goblet/Enterocyte)
cE08 (Goblet)
cE09 (Best4)
cE10 (Tuft)
cE11 (Enteroendocrine)
f
PTK2 Expression in tumor cell
g
avg.exp
pct.exp
MMRp
MMRd
MMRp Normal
MMRd Normal
h
Average Expression
Percent Expressed
PTK2
i
Human CRC
Adjacent normal
Tumor
FAK
p-FAK
200 μm
% of FAK+Area
% of pFAK+Area
P < 0.0001
j
Intratumoral
Pearson r = 0.8382
P = 0.0093
% of PD-1 expression
% of p-FAK area
Pearson r = 0.8574
P = 0.0065
% ofTIM-3 expression
Pearson r = 0.5409
P = 0.1663
% of LAG-3 expression
k
DAPI/CK19
DAPI/pFAK
DAPI/CD3
DAPI/TIM-3
l
pFAK high
pFAK low
mIHC
Phenotype map
Intratumoral
Proximal
Distal
200 μm
TIM-3+ TILs (<100 μm)
TIM-3+ TILs (>100 μm)
Proximity line (100 μm)
pFAK+ CK19+ tumor cells
m
pFAK+ cells
% All cells
P < 0.0001
n
TIM-3+ TILs
% All cells
P < 0.0001
o
TIM-3+ TILs
(<100 μm to pFAK+CK19+ cells)
% TIM-3+ TILs
P < 0.0001
pFAK high
pFAK low
p
TIM-3+cells
Tumor
100 μm
pFAK high
pFAK low

Figure 3

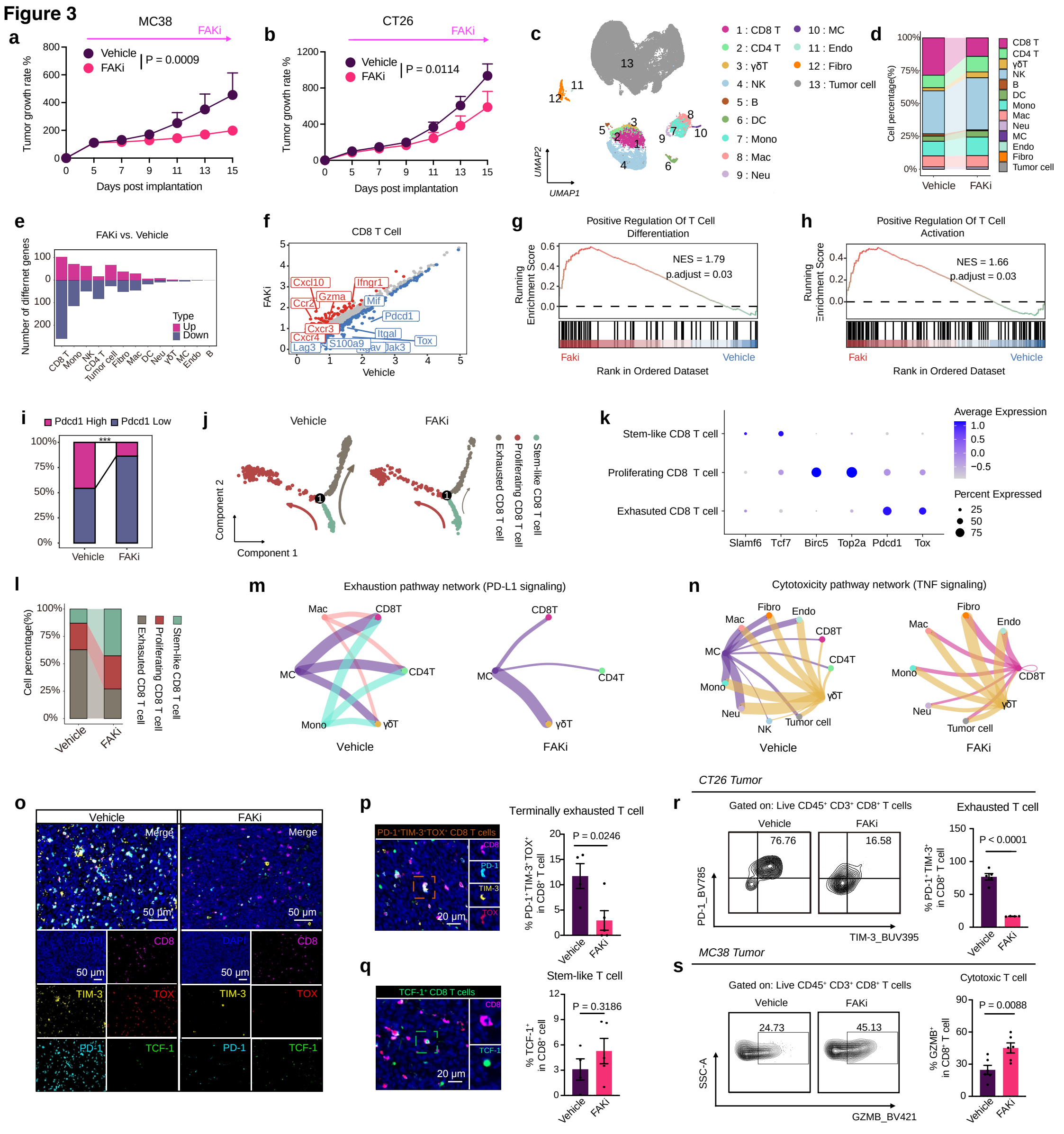
a
MC38
FAKi
Vehicle
FAKi
P = 0.0009
Tumor growth rate %
Days post implantation
b
CT26
FAKi
Vehicle
FAKi
P = 0.0114
Tumor growth rate %
Days post implantation
c
1 : CD8 T
2 : CD4 T
3 : γδT
4 : NK
5 : B
6 : DC
7 : Mono
8 : Mac
9 : Neu
10 : MC
11 : Endo
12 : Fibro
13 : Tumor cell
UMAP2
UMAP1
d
Cell percentage(%)
Vehicle
FAKi
CD8 T
CD4 T
γδT
NK
B
DC
Mono
Mac
Neu
MC
Endo
Fibro
Tumor cell
e
FAKi vs. Vehicle
Number of differnet genes
Type
Up
Down
CD8 T
Mono
NK
CD4 T
Tumor cell
Fibro
Mac
DC
Neu
γδT
MC
Endo
B
f
CD8 T Cell
FAKi
Vehicle
Cxcl10
Ifngr1
Gzma
Ccr2
Mif
Pdcd1
Cxcr3
Itgal
Cxcr4
Tox
Lag3
S100a9
Jak3
g
Positive Regulation Of T Cell Differentiation
Running Enrichment Score
NES = 1.79
p.adjust = 0.03
Faki
Vehicle
Rank in Ordered Dataset
h
Positive Regulation Of T Cell Activation
Running Enrichment Score
NES = 1.66
p.adjust = 0.03
Faki
Vehicle
Rank in Ordered Dataset
i
Pdcd1 High
Pdcd1 Low
***
Vehicle
FAKi
j
Vehicle
FAKi
Component 2
Component 1
Exhausted CD8 T cell
Proliferating CD8 T cell
Stem-like CD8 T cell
k
Stem-like CD8 T cell
Proliferating CD8 T cell
Exhasuted CD8 T cell
Slamf6
Tcf7
Birc5
Top2a
Pdcd1
Tox
Average Expression
Percent Expressed
l
Cell percentage(%)
Exhasuted CD8 T cell
Proliferating CD8 T cell
Stem-like CD8 T cell
Vehicle
FAKi
m
Exhaustion pathway network (PD-L1 signaling)
Mac
CD8T
MC
CD4T
Mono
γδT
Vehicle
CD8T
MC
CD4T
γδT
FAKi
n
Cytotoxicity pathway network (TNF signaling)
Fibro
Endo
Mac
CD8T
MC
CD4T
Mono
γδT
Neu
NK
Tumor cell
Vehicle
Fibro
Endo
Mac
Mono
CD8T
γδT
Neu
Tumor cell
FAKi
o
Vehicle
FAKi
Merge
50 μm
DAPI
CD8
TIM-3
TOX
PD-1
TCF-1
p
PD-1+TIM-3+TOX+ CD8 T cells
CD8
PD-1
TIM-3
TOX
20 μm
Terminally exhausted T cell
P = 0.0246
% PD-1+TIM-3+TOX+ in CD8+ T cell
Vehicle
FAKi
q
TCF-1+ CD8 T cells
CD8
TCF-1
20 μm
Stem-like T cell
P = 0.3186
% TCF-1+ in CD8+ T cell
Vehicle
FAKi
r
CT26 Tumor
Gated on: Live CD45+ CD3+ CD8+ T cells
Vehicle
FAKi
76.76
16.58
PD-1_BV785
TIM-3_BUV395
Exhausted T cell
P < 0.0001
% PD-1+TIM-3+ in CD8+ T cell
Vehicle
FAKi
s
MC38 Tumor
Gated on: Live CD45+ CD3+ CD8+ T cells
Vehicle
FAKi
24.73
45.13
SSC-A
GZMB_BV421
Cytotoxic T cell
P = 0.0088
% GZMB+ in CD8+ T cell
Vehicle
FAKi

Figure 4

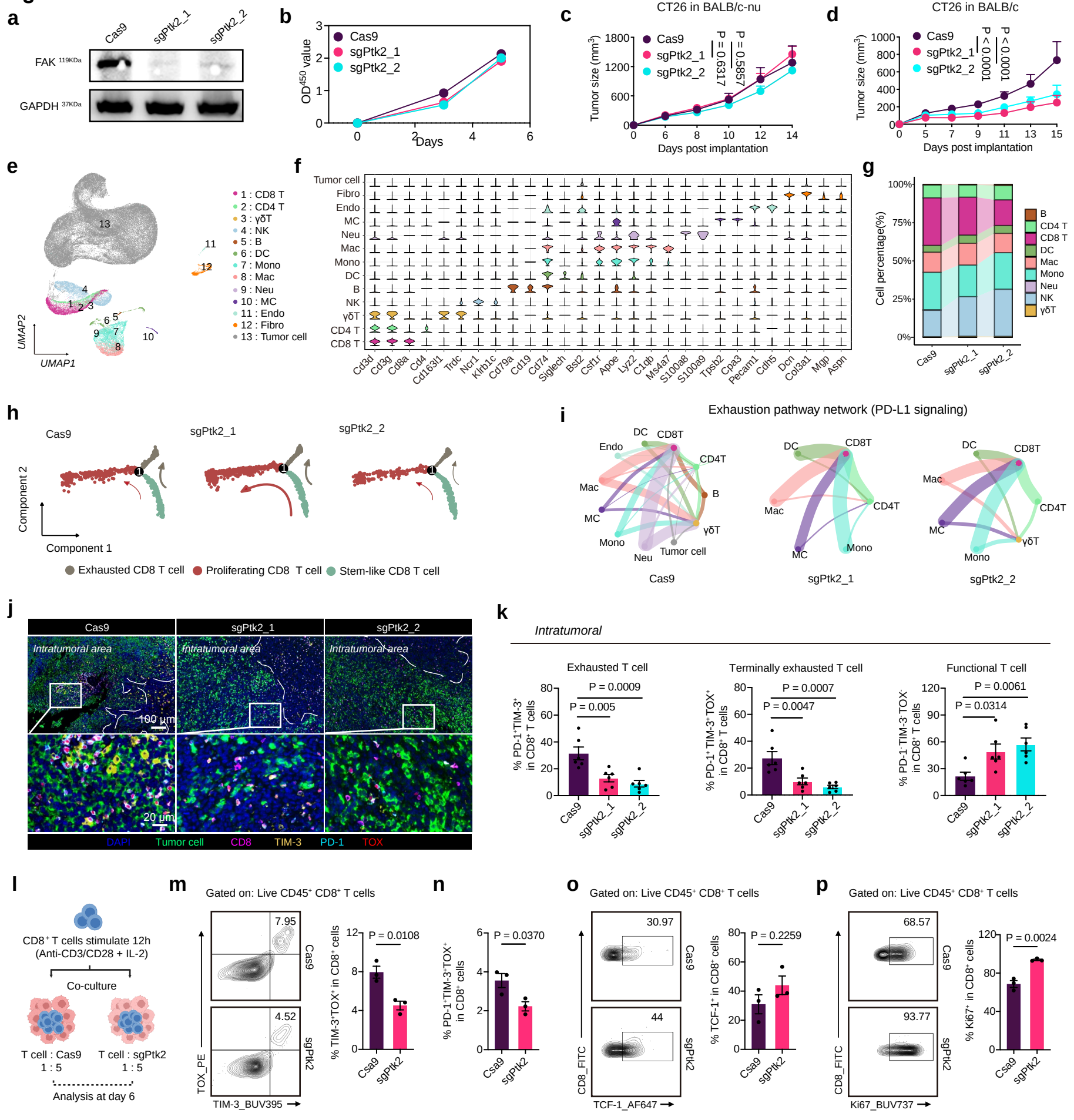
a
Cas9
sgPtk2_1
sgPtk2_2
FAK 119KDa
GAPDH 37KDa
b
Cas9
sgPtk2_1
sgPtk2_2
OD450 value
Days
c
CT26 in BALB/c-nu
Tumor size (mm3)
P = 0.6317
P = 0.5857
Days post implantation
d
CT26 in BALB/c
P < 0.0001
P < 0.0001
Days post implantation
e
1 : CD8 T
2 : CD4 T
3 : γδT
4 : NK
5 : B
6 : DC
7 : Mono
8 : Mac
9 : Neu
10 : MC
11 : Endo
12 : Fibro
13 : Tumor cell
UMAP1
UMAP2
f
Tumor cell
Fibro
Endo
MC
Neu
Mac
Mono
DC
B
NK
γδT
CD4 T
CD8 T
Cd3d Cd3g Cd8a Cd4 Cd163l1 Trdc Ncr1 Klrb1c Cd79a Cd19 Cd74 Siglech Bst2 Csf1r Apoe Lyz2 C1qb Ms4a7 S100a8 S100a9 Tpsb2 Cpa3 Pecam1 Cdh5 Dcn Col3a1 Mgp Aspn
g
Cell percentage(%)
B
CD4 T
CD8 T
DC
Mac
Mono
Neu
NK
γδT
Cas9
sgPtk2_1
sgPtk2_2
h
Cas9
sgPtk2_1
sgPtk2_2
Component 2
Component 1
Exhausted CD8 T cell
Proliferating CD8 T cell
Stem-like CD8 T cell
i
Exhaustion pathway network (PD-L1 signaling)
DC
CD8T
Endo
CD4T
Mac
B
MC
γδT
Mono
Neu
Tumor cell
Cas9
sgPtk2_1
sgPtk2_2
j
Cas9
sgPtk2_1
sgPtk2_2
Intratumoral area
100 μm
20 μm
DAPI
Tumor cell
CD8
TIM-3
PD-1
TOX
k
Intratumoral
Exhausted T cell
Terminally exhausted T cell
Functional T cell
P = 0.0009
P = 0.005
P = 0.0007
P = 0.0047
P = 0.0061
P = 0.0314
% PD-1+TIM-3+ in CD8+ T cells
% PD-1+TIM-3+TOX+ in CD8+ T cells
% PD-1-TIM-3-TOX- in CD8+ T cells
Cas9
sgPtk2_1
sgPtk2_2
l
CD8+ T cells stimulate 12h
(Anti-CD3/CD28 + IL-2)
Co-culture
T cell : Cas9
1 : 5
T cell : sgPtk2
1 : 5
Analysis at day 6
m
Gated on: Live CD45+ CD8+ T cells
7.95
4.52
Cas9
sgPtk2
TOX_PE
TIM-3_BUV395
P = 0.0108
% TIM-3+TOX+ in CD8+ cells
Csa9
sgPtk2
n
P = 0.0370
% PD-1+TIM-3+TOX+ in CD8+ cells
Csa9
sgPtk2
o
Gated on: Live CD45+ CD8+ T cells
30.97
44
Cas9
sgPtk2
CD8_FITC
TCF-1_AF647
P = 0.2259
% TCF-1+ in CD8+ cells
Csa9
sgPtk2
p
Gated on: Live CD45+ CD8+ T cells
68.57
93.77
Cas9
sgPtk2
CD8_FITC
Ki67_BUV737
P = 0.0024
% Ki67+ in CD8+ cells
Csa9
sgPtk2

Figure 5

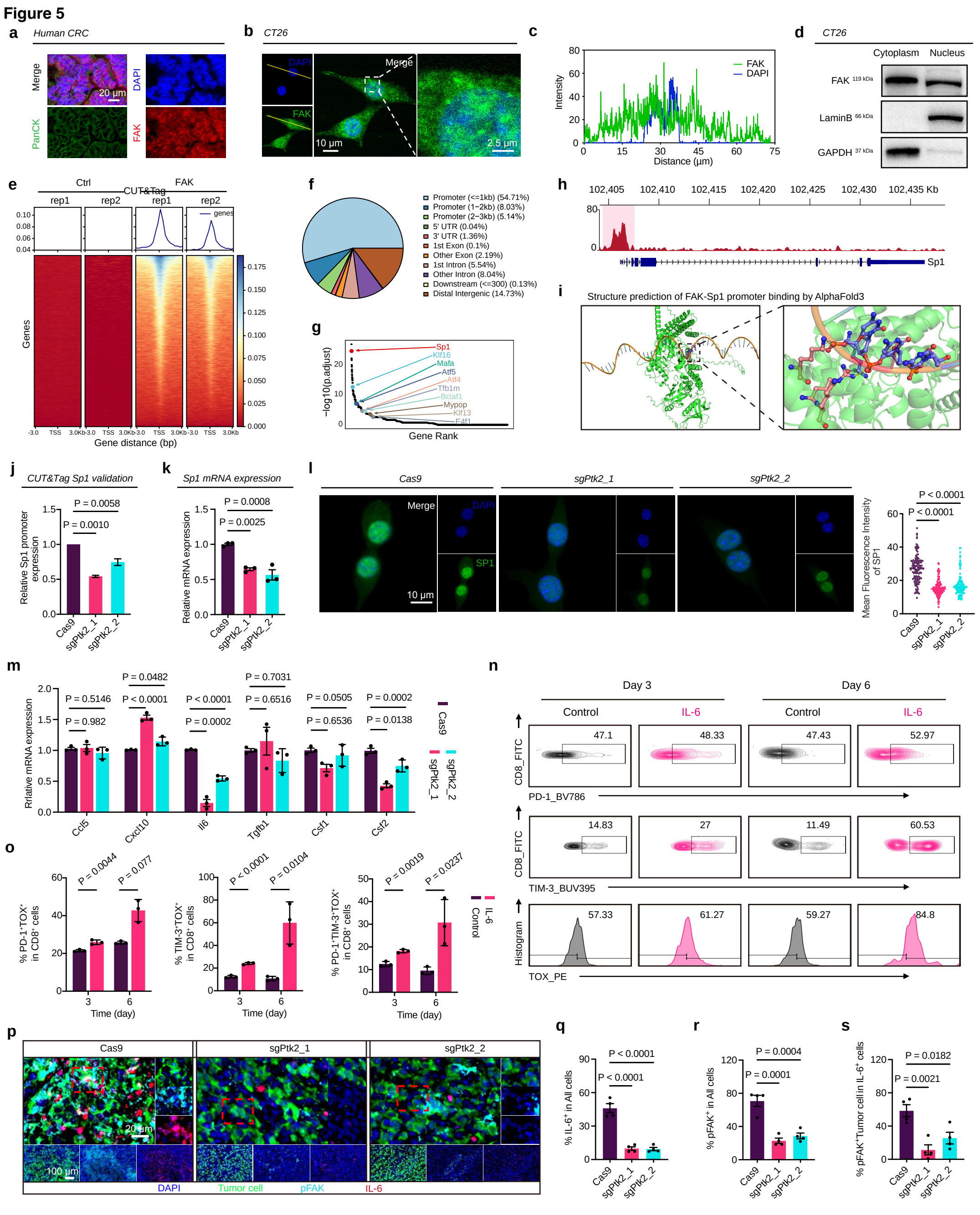
a
Human CRC
Merge
DAPI
PanCK
FAK
20 μm
b
CT26
DAPI
FAK
Merge
10 μm
2.5 μm
c
Intensity
Distance (μm)
FAK
DAPI
d
CT26
Cytoplasm
Nucleus
FAK 119 kDa
LaminB 66 kDa
GAPDH 37 kDa
e
Ctrl
FAK
CUT&Tag
rep1
rep2
genes
Genes
Gene distance (bp)
f
Promoter (<=1kb) (54.71%)
Promoter (1−2kb) (8.03%)
Promoter (2−3kb) (5.14%)
5' UTR (0.04%)
3' UTR (1.36%)
1st Exon (0.1%)
Other Exon (2.19%)
1st Intron (5.54%)
Other Intron (8.04%)
Downstream (<=300) (0.13%)
Distal Intergenic (14.73%)
g
−log10(p.adjust)
Gene Rank
Sp1
Klf16
Mafa
Atf5
Atf4
Tfb1m
Bclaf1
Mypop
Klf13
E4f1
h
102,405
102,410
102,415
102,420
102,425
102,430
102,435 Kb
Sp1
i
Structure prediction of FAK-Sp1 promoter binding by AlphaFold3
j
CUT&Tag Sp1 validation
Relative Sp1 promoter expression
P = 0.0058
P = 0.0010
Cas9
sgPtk2_1
sgPtk2_2
k
Sp1 mRNA expression
Relative mRNA expression
P = 0.0008
P = 0.0025
l
Cas9
sgPtk2_1
sgPtk2_2
Merge
DAPI
SP1
10 μm
Mean Fluorescence Intensity of SP1
P < 0.0001
P < 0.0001
m
Rrlative mRNA expression
P = 0.5146
P = 0.982
P = 0.0482
P < 0.0001
P < 0.0001
P = 0.0002
P = 0.7031
P = 0.6516
P = 0.0505
P = 0.6536
P = 0.0002
P = 0.0138
Ccl5
Cxcl10
Il6
Tgfb1
Csf1
Csf2
Cas9
sgPtk2_1
sgPtk2_2
n
Day 3
Day 6
Control
IL-6
CD8_FITC
PD-1_BV786
TIM-3_BUV395
Histogram
TOX_PE
47.1
48.33
47.43
52.97
14.83
27
11.49
60.53
57.33
61.27
59.27
84.8
o
% PD-1+TOX+ in CD8+ cells
% TIM-3+TOX+ in CD8+ cells
% PD-1+TIM-3+TOX+ in CD8+ cells
P = 0.0044
P = 0.077
P < 0.0001
P = 0.0104
P = 0.0019
P = 0.0237
Time (day)
Control
IL-6
p
Cas9
sgPtk2_1
sgPtk2_2
20 μm
100 μm
DAPI
Tumor cell
pFAK
IL-6
q
% IL-6+ in All cells
P < 0.0001
P < 0.0001
r
% pFAK+ in All cells
P = 0.0004
P = 0.0001
s
% pFAK+Tumor cell in IL-6+ cells
P = 0.0182
P = 0.0021

Figure 6

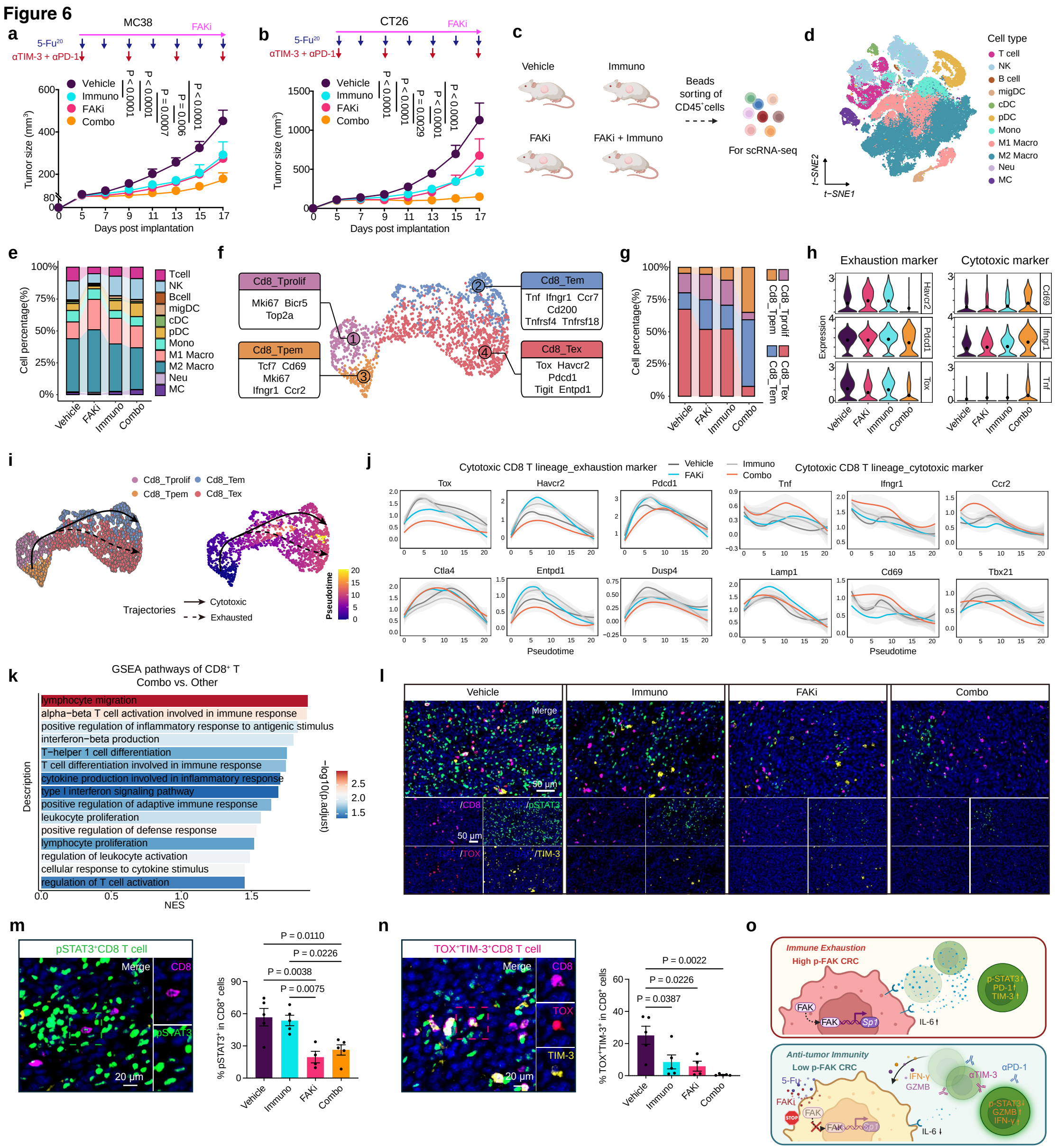
a
MC38
FAKi
5-Fu20
αTIM-3 + αPD-1
Vehicle
Immuno
FAKi
Combo
P < 0.0001
P < 0.0001
P = 0.0007
P = 0.006
P < 0.0001
Tumor size (mm3)
Days post implantation
b
CT26
FAKi
5-Fu20
αTIM-3 + αPD-1
P < 0.0001
P < 0.0001
P = 0.0029
P < 0.0001
P < 0.0001
Tumor size (mm3)
Days post implantation
c
Vehicle
Immuno
FAKi
FAKi + Immuno
Beads sorting of CD45+cells
For scRNA-seq
d
Cell type
T cell
NK
B cell
migDC
cDC
pDC
Mono
M1 Macro
M2 Macro
Neu
MC
t−SNE2
t−SNE1
e
Cell percentage(%)
Tcell
NK
Bcell
migDC
cDC
pDC
Mono
M1 Macro
M2 Macro
Neu
MC
Vehicle
FAKi
Immuno
Combo
f
Cd8_Tprolif
Mki67 Bicr5
Top2a
Cd8_Tem
Tnf Ifngr1 Ccr7
Cd200
Tnfrsf4 Tnfrsf18
Cd8_Tpem
Tcf7 Cd69
Mki67
Ifngr1 Ccr2
Cd8_Tex
Tox Havcr2
Pdcd1
Tigit Entpd1
g
Cell percentage(%)
Cd8_Tprolif
Cd8_Tpem
Cd8_Tem
Cd8_Tex
Vehicle
FAKi
Immuno
Combo
h
Exhaustion marker
Cytotoxic marker
Havcr2
Pdcd1
Tox
Cd69
Ifngr1
Tnf
Expression
Vehicle
FAKi
Immuno
Combo
i
Cd8_Tprolif
Cd8_Tem
Cd8_Tpem
Cd8_Tex
Trajectories
Cytotoxic
Exhausted
Pseudotime
j
Cytotoxic CD8 T lineage_exhaustion marker
Vehicle
FAKi
Immuno
Combo
Cytotoxic CD8 T lineage_cytotoxic marker
Tox
Havcr2
Pdcd1
Tnf
Ifngr1
Ccr2
Ctla4
Entpd1
Dusp4
Lamp1
Cd69
Tbx21
Pseudotime
Pseudotime
k
GSEA pathways of CD8+ T
Combo vs. Other
lymphocyte migration
alpha−beta T cell activation involved in immune response
positive regulation of inflammatory response to antigenic stimulus
interferon−beta production
T−helper 1 cell differentiation
T cell differentiation involved in immune response
cytokine production involved in inflammatory response
type I interferon signaling pathway
positive regulation of adaptive immune response
leukocyte proliferation
positive regulation of defense response
lymphocyte proliferation
regulation of leukocyte activation
cellular response to cytokine stimulus
regulation of T cell activation
Description
NES
−log10(p.adjust)
l
Vehicle
Immuno
FAKi
Combo
Merge
50 μm
DAPI /CD8
DAPI /pSTAT3
DAPI /TOX
DAPI /TIM-3
m
pSTAT3+CD8 T cell
Merge
CD8
pSTAT3
20 μm
P = 0.0110
P = 0.0226
P = 0.0038
P = 0.0075
% pSTAT3+ in CD8+ cells
Vehicle
Immuno
FAKi
Combo
n
TOX+TIM-3+CD8 T cell
Merge
CD8
TOX
TIM-3
20 μm
P = 0.0022
P = 0.0226
P = 0.0387
% TOX+TIM-3+ in CD8+ cells
Vehicle
Immuno
FAKi
Combo
o
Immune Exhaustion
High p-FAK CRC
FAK
Sp1
IL-6
p-STAT3
PD-1
TIM-3
Anti-tumor Immunity
Low p-FAK CRC
5-Fu
FAKi
STOP
IFN-γ
GZMB
αTIM-3
αPD-1
p-STAT3
GZMB
IFN-γ
IL-6